2008

MICRO-CT MATERIAL INTERPRETATION BY SEGMENTATION AND MULTI-ENERGY DATA ACQUISITION

Patrick V. Granton

MICRO-CT MATERIAL INTERPRETATION BY SEGMENTATION AND MULTI-ENERGY DATA ACQUISITION

(Spine title: Multi-Energy Micro-Computed Tomography)

(Thesis Format: Integrated-Article)

by

Patrick V. Granton

Graduate Program in
Physics and Astronomy

Submitted in partial fulfillment
of the requirements for the degree of
Master of Science

The School of Graduate and Postdoctoral Studies
The University of Western Ontario
London, Ontario

Abstract

Micro-CT is a 3-D non-invasive high-resolution imaging tool, which is often used for visualizing anatomical features in small animals. Micro-CT generates 3-D grey-scale anatomical images based on X-ray attenuation differences between tissues. The rapid growth in micro-CT imaging systems and recent advances in micro-CT technology have made it an excellent tool for quantifying tissues, based on their CT image intensity alone. In this thesis we have imaged entire rats and quantified their whole-body composition of adipose tissue (fat), lean tissue (organs), and bone using a rapid cone-beam flat-panel micro-CT system. However, this technique is limited in situations where exogenous contrast agents are introduced, due to the similar X-ray attenuation values, which are exhibited by typical contrast agents and cortical bone. By imaging a rat specimen (containing a lead-based vascular contrast) at more than one X ray energy, we have overcome this limitation and decomposed conventional post-reconstructed micro-CT images to form 3-D independent images of vessels, bone and soft-tissue.

Keywords: body composition, cone-beam micro-CT, dual-energy CT, triple-energy CT, *K*-edge imaging

Co-authorship

The following thesis is formatted as an integrated-article style, containing four chapters. The first and fourth chapter (introduction and conclusion), are documents that do not involve any co-authors. The second chapter in my thesis entitled, "*Rapid In Vivo Whole-body Composition of Rats From Cone-Beam Micro-CT*" is in preparation for publication and the sequential author list is: Patrick V. Granton, Chris Norley, Joseph Umoh, and David W. Holdsworth. My role in this document included: micro-CT imaging of the dead rodent specimens, image processing, image analysis, and preparing the written text in this chapter. Joseph Umoh imaged the live rodent specimens. Chris Norley and David W. Holdsworth edited the document. A version of the third chapter of my thesis has been submitted to Medical Physics for publication. The submitted full title of this paper for publication is, "*Implementation Of Dual- and Triple-Energy Cone-Beam Micro-CT for Post-Reconstruction Material Decomposition.*" Authors to this paper are sequentially: Patrick V. Granton, Steve I. Pollmann, Nancy L. Ford, Maria Drangova, and David W. Holdsworth. My role in this paper (which incorporates the primary work of the master's study) is as follows: I conducted all of the background research, performed the computer simulation modeling, imaging, image analysis, and wrote the text. Steve I. Pollmann wrote code in C++ to perform the image analysis component of the chapter. Nancy L. Ford assisted in running the imaging experiments. Steve I. Pollmann, Maria Drangova, and David W. Holdsworth, all contributed to the final document through peer revision, editing, and advice.

Epigraph

"I have been impressed with the urgency of doing. Knowing is not enough; we must apply. Being willing is not enough; we must do." – Leonardo da Vinci

Dedication

This work is dedicated to my parents Vince J. and Pauline H. Granton for their support and encouragement as well as in memory to my late grandmother Marie Collett (1919-2006) and my departed colleague Louise Du (1980 – 2007).

Acknowledgements

I would like to acknowledge those individuals who have offered their support and guidance during my period at John P. Robarts research laboratories, and at the department of Physics and Astronomy at the University of Western Ontario.

I would like to start by thanking my supervisor, David W. Holdsworth for the opportunity to be apart of his research group, known for its high caliber of scientific proficiency. It has been truly an honour to work under his guidance and to learn from of his superior approach to scientific research and publications.

Logistically, the work presented herein could not have been preformed without contributions from Lanette Freeson and her laboratory specimen; as well as financial contributions provided by the Canadian Institutes of Health Research (MOP-67018, IMH-67018) and the Ontario Research and Development Challenge Fund.

Within the Imaging Lab there are several individuals I would like to thank, particularly: Maria Drangova, Hristo Nikolo, Chris Norley, Steve Pollmann, and Joseph Umoh for their assistance, guidance, and general friendship.

It cannot go without saying but the scientific discussions I've held and technical assistance I've received from my former colleague Louise Du, a skilled scientist, will live on in any scientific contributions that I make in the future and she will be forever missed.

Finally, this work could not have been accomplished without the love and support (both financially and motivationally) provided to me from my parents, whom I feel lucky to have.

Table of Contents

List of Tables

List of Figures

List of Abbreviations

Micro-CT – Micro Computed Tomography
PET – Positron Emission Tomography
SPET – Single Photon Emission Tomography
MRI – Magnetic Resonance Imaging
FOV – Field of View
ROI – Region of Interest
LAC – Linear Attenuation Coefficient
CCD – Charged Coupled Device
Voxel – Volume Element
SED – Sedentary Bred
DSE – Daily Spontaneous Exercise
BMC – Bone Mineral Content
BMD – Bone Mineral Density
AT – Adipose Tissue
LT – Lean Tissue
CMCR – Contrast of Microfil to Cortical Bone Ratio
HU – Hounsfeld Units
kVp – Peak Kilovoltage
DECT – Dual-Energy Computed Tomography
DSCT – Dual-Source Computed Tomography

Chapter 1: INTRODUCTION

1.1 Non-Invasive Imaging

1.1.1 Motivation for Non-Invasive Imaging in Small Animal Studies

Animal research models have led to innumerable advances in medical knowledge and treatment of disease, such as in leukaemia,[1] diabetes,[2] and polio,[3] amongst others. For example, new drugs may only progress to clinical trials if the metabolic interactions relating to its safety and toxicity are known—which in large part can only be understood using animals. More specifically, the use of rodents or small animals makes up the majority of all animal studies (84%) in pre-clinical disease investigations.[3]

In addressing the pressing and immediate need for the diagnosis and treatment of many common human ailments, a powerful tool used by physicians and care providers is non-invasive 3-D anatomical imaging; such as Computed Tomography (CT) or Magnetic Resonance Imaging (MRI). More recently, non-invasive imaging has evolved and been adapted from applications in humans, for use in small animal research models.[4-6] These imaging devices differ from their clinical counterparts most notably by a considerable increase in image resolution.[7,8] One way in which disease investigations involving small animals benefit from imaging developed for human use is by being able to easily translate from basic to clinical investigations without any major experimental paradigm shift.

Prior to the development of non-invasive small animal imaging, traditional disease investigations using small animals involved invasive biopsies or relied on assays

obtained from blood or urine.[9] Non-invasive imaging improves preclinical small animal studies over previous methods through targeted longitudinal *in vivo* studies of the biological region of interest (ROI). Furthermore, the ability to examine animals *in vivo,* over an extended period of time, eliminates the need to immediately sacrifice animal subjects and ultimately reduces the required number of subjects and associated costs.[5]

There are a number of non-invasive 3-D imaging technologies available for small animal imaging. Technologies such as: single photon emission computed tomography (SPECT), micro-CT, high-resolution MRI, positron emission tomography (PET) and emerging 3-D ultrasound[10], have made a considerable impact on disease understanding, particularly in oncological studies.[4,6,11] However, no one imaging modality will provide a complete picture of a particular disease model, and as is often the case, disease expression is usually characterized by several imaging modalities.

It is important to understand the strengths and limitations of each imaging modality, such that the resulting data ultimately enhances the understanding of a particular disease model. If limitations do exist, and they are not fundamental physical limitations, then technological progress can be used to further extend the possibilities of each imaging modality. This thesis will examine the imaging modality of micro-CT, and aims to improve its ability to obtain accurate and precise measurements in preclinical experiments. In addition, it will demonstrate a new technique to overcome a limitation of micro-CT image data to distinguish between two different materials that share similar grey-scale image intensity.

1.2 Micro-CT: Imaging Technology

1.2.1 Existing Capabilities of Micro-CT Imaging

Micro-CT has been established as an excellent high-resolution computational and qualitative imaging tool for investigating bone architecture, bone mineral density, and visualizing anatomical spatial orientation in small animals.[12,13] Micro-CT generates 3-D grey-scale image volumes of animal subjects based on X-ray attenuation differences between tissues. In general, dense tissues (or tissues having components high in atomic number, such as bone) preferentially attenuate X rays. This makes micro-CT highly sensitive in resolving bone architecture from surrounding tissue and well-suited to detect bone lesions.[14] Additionally, by acquiring volumetric images of highly detailed bone anatomy such as trabecular struts, finite elemental models can be generated from the 3-D micro-CT image data to reveal structural information.[15]

Micro-CT image data containing bony anatomy can also provide an equivalent bone mineral content (in grams) by correlating signal intensities to known concentrations of a bone-mimicking material, such as calcium carbonate. Since CT is a volumetric imaging method, by calculating the bone mineral content in specific regions we can calculate a bone mineral density (BMD) for a region of interest (ROI), such as a femur, or a whole skeleton in a rodent.

Note that the use of the words micro-CT and CT are used interchangeably throughout this thesis, except when describing a particular imaging system in which a distinction is made. The distinction between micro-CT and CT is primarily considered in image resolution, i.e. the spacing between volume elements or voxels in the final 3-D

digital image. X-ray imaging systems wth isotropic voxels spacings near 200 μm are considered data obtained from a micro-CT imaging device, while those greater than 200 μm are considered data obtain from a CT or clinical CT scanner.

At nominal spatial resolutions of 200 μm or less, micro-CT provides superior visualization for identifying anatomical features in small animals, such as organs or tumours and their spatial relationship with surrounding tissues. In addition, anatomical features can be quantitatively analyzed to report measurements like organ volumes such as in the heart,[16] or the lungs.[17]

Despite the known difficulty of CT to provide adequate contrast between soft tissue types – due to the similarity of their X-ray transmission quality – CT has been shown to quantitatively distinguish adipose tissue (fat) from lean tissue (muscle) well in humans and small animals.[18]

1.2.2 Contrast Agents in CT

In some circumstances, the difficulty of CT image data to distinguish between soft tissues can be overcome through into the biological introduction of radiopaque contrast agents.[19] These exogenous materials, generally containing elements high in atomic number, can be introduced into a biological specimen intravenously,[20] injected into the inter-tissue space, [21] or injected orally.[22] For live specimens, these contrast agents are chelated – a process in which the contrast agent is made biologically safe by being bound to a ligand before being introduced into the subject.

Most contrast agents introduced into the blood stream are removed rapidly through the kidney. However, more recently developed larger macromolecule contrast agents can remain in the blood stream for several hours and are removed via phagocytosis or the hepatobiliary pathway.[23,24] Typical contrast mediums used in clinical and pre-clinical live-animal studies are barium or iodine based. Additional radiographic applications using contrast agents include: blood-flow perfusion, renal function quantification, and the illumination of tumours or vessel occlusions in stroke-risk patients.[25]

However, the biological introduction of any exogenous compound is potentially harmful, depending on its toxicity and physiochemotoxicity, which can lead to complications or even death. Even the Food and Drug Administration's (FDA, USA) approved contrast agents for use in humans have an etiology that could lead to nephropathy,[26] thromboembolism or angina.[27] Since the metabolic and chemical interactions of newly introduced contrast agents are not well biologically understood, their widespread use is highly regulated. Thus, the current chemical variety of contrast agents for humans and live animals is limited. However, in pre-clinical small animal studies, including sacrificed animal specimens, a large variety of chemically based contrast agents can be biologically introduced and potentially explored, such as those using strontium,[28] or lead-based contrast media.[29]

1.2.3 Micro-CT Limitations: Case for Dual- or Multi-Energy CT

Despite the extended capabilities of radiographic applications through contrast agents, a limitation of CT is that two different materials may share similar grey-scale values, making it difficult to perform image segmentation based on grey-scale signal intensity alone. Also a related CT ambiguity remains, for example a CT image of a breast containing a lesion and exhibiting an increased single intensity from the surrounding tissue may be a result of either calcification (changes in composition), changes in density or a combination of the two.

Dual-energy computed tomography (DECT) has been shown to decompose CT grey-scale intensity values into both effective atomic number and electron density; or into the relative abundances of three pre-defined basis materials.[30-33] Dual-energy techniques exploit the fact that, in the diagnostic energy range, there are two main independent attenuation processes: the photoelectric effect and Compton scattering. The relative role of these processes depends on the atomic number and electron density of the material. By acquiring attenuation information about a specimen at two energies (i.e. one at an energy where the photoelectric effect dominates, and the other at an energy where Compton scattering dominates), we can decompose CT data to reveal compositional information.

1.2.4 *K*-edge Imaging and multiple energies

An additional aspect of the photoelectric effect occurs when tightly bound electrons are liberated, causing sharp and significant changes in X-ray attenuation. For *K*-shell electrons, the energy at which this occurs is called the *K* edge. Materials with higher atomic numbers (>40), exhibit a *K* edge within the diagnostic energy range and can be distinguished from surrounding tissue by acquiring X-ray attenuation information at energies that straddle their *K* edge.[34] Furthermore, multiple X ray attenuation measurements could possibly improve material decomposition of CT data in the presence of *K* edges, analogous to chemical interpretation via emission spectroscopy. X-ray imaging using multiple energies sensitive to an element's *K* edge (a process referred to as *K*-edge imaging) had been explored as early as the 1980's where efforts have focused on isolating iodinated contrast agents in fluoroscopic video images,[35] digital subtraction radiography,[36,37] and CT[34,38,39] with some success.

Continued explorations in novel CT applications involving *K*-edge imaging or dual-energy approaches had until recently stagnated, but renewed interest with the introduction of clinical dual X-ray source CT has reignited this field.[40] A backlog of recent and past theoretical work, including the use of multiple energy-dependent attenuation data for material analysis will likely begin to be applied in clinical applications; as has been recently proposed using iodine and gadolinium contrast-agents.[34]

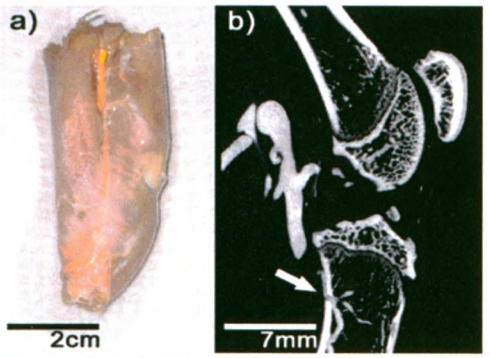

Figure 1-1 *(a) Excised Sprague-Dawley rat leg profused with Microfil (yellow). (b) Micro-CT image slice showing the similarity of contrast-enhanced vessel near bone (arrow).*

Of particular interest for material decomposition using multi-energy imaging is a lead-based contrast agent called Microfil (MV-122, Flow Tech, Carver, MA). Microfil is a radiopaque contrast agent composed of silicone rubber doped with lead sulfate and lead chromate. It is perfused into non-surviving animal specimens under physiological pressure for vascular visualization. Micro-CT-based applications using Microfil have been used to investigate the renal vasculature of rats[41] and cardiovascular system of embryonic birds.[42] However, in regions where vessel meets bone, vessel segmentation by grey-scale intensity alone fails, since the intensity values of bone are too similar to the contrast-enhanced vessels (as seen in **Figure 1-1**). [29]

1.2.5 Dual-Energy and *K*-edge Imaging Techniques

There are a variety of ways to acquire dual- or multi-energy attenuation data for material decomposition. For example, either a dual-energy detector,[43] or a dual-energy X-ray beam source[40] could be used to acquire measurements of the attenuation data for a given object. Furthermore, material decomposition techniques can be applied to the projection data or in the post-reconstructed volumetric data. However, in practical implementation of multi-energy CT data acquisition, a number of technical considerations should be taken into account. As well, a more thorough understanding of the physical basis for material decomposition is required in order to optimize data acquisition, given the constraints and parameters of typical micro-CT imaging systems.

1.3 Micro-CT: A Technical Understanding

1.3.1 X ray Imaging Principles and Technology

As alluded to earlier, the majority of X-ray imaging systems (like CT) fundamentally measure line integrals of photon transmission through an object from an X-ray source to an X-ray detector in order to form an image. For humans and small animals, diagnostically relevant X-rays occur at energies ranging from 20 to 140 KeV. Photons at these energies can liberate bound electrons and are therefore considered a form of ionizing radiation which deposit energy to the imaged object or specimen, quantified in the term *dose*, measured in units of Gray (J/Kg).

The relative probability of interaction for a monochromatic X-ray photon beam passing through a uniform thickness of material is called the linear attenuation coefficient (L.A.C.), denoted by μ (cm^{-1}). The total path transmission of X rays through a material is known to exponentially diminish, dependent upon on the product of a material's linear attenuation coefficient (μ) and the material thickness (d). This is defined by the Lambert-Beer law as:

$$I = I_o e^{-(\mu d)} \qquad [1].$$

In equation 1, I_o is the incident photon intensity and I is the transmitted photon intensity. For most CT systems the incident photon intensity is measured prior to placing an object in front of the detector, called a bright field, while a second measurement is taken with the object in front of the detector, providing, I_o and I, respectively. By taking

the natural logarithm in equation (1) one can solve for μd or X ray transmission measurement in a CT projection as,

$$\mu d = \ln\left(\frac{I_o}{I}\right) \qquad [2].$$

Since each transmission measurement along a ray path through a material can be considered to be equivalently the sum of attenuation due to a number of uniform finite thicknesses Δx through a material of thickness d, we can alternatively express equation 2 as,

$$\mu d = \mu_1 \Delta x + \mu_2 \Delta x + \mu_3 \Delta x + \ldots \mu_N \Delta x \qquad \text{or,}$$

$$\mu d = \Delta x \sum_{i}^{N} (\mu_N(x)) \qquad [3].$$

In a single CT projection, many transmission measurements along ray paths are acquired in individual detector elements, the amount of which depends on the CT generation and detector type. The goal of CT is to acquire a sufficient number of transmission values at each projection view angle through an object – acquired around a single axis of rotation spaced at angular increments – such that we can solve and form computationally, a 3-D digital representation of the linear attenuation coefficients of that object. The Δx as expressed in 3-D, is a representation of the nominal resolution or isotropic voxel spacing, determined largely from the size of uniform detector elements, and on geometric magnification in fan-or cone-beam CT scanners.

In order to communicate the L.A.C.s relating to specific materials in a meaningful and standardized way, CT data is scaled in Hounsfeld units, such that air corresponds to

an attenuation value of -1000 HU, water to a value of 0 HU, and all other materials scaled linearly according to this calibration. In this framework, cortical bone generally has a CT value of approximately 2000 HU.

The linear attenuation coefficient, or attenuation likelihood, is as one might expect, dependent on the energy of the photon; for instance, optical light does not penetrate through the human body. As a consequence of the energy dependence in $\mu(E)$, lower energy X rays are preferentially filtered in an X-ray spectrum, resulting in an image artefact known as beam hardening.

1.3.2 X ray Attenuation Mechanisms

By understanding the physical mechanisms that contribute to the linear attenuation coefficients one can interpret, both qualitatively and quantitatively, the composition of an imaged object or imaged specimen. However, an analytical derivation by first principles of the contributing physical mechanisms to the L.A.C.s is complex and beyond the scope of this thesis, such that an abridged summary of the dominant mechanisms is presented.

In the diagnostic energy regime, incident photons in the X-ray beam are primarily absorbed or deflected by three independent mechanisms; coherent (or Raleigh) scattering; the photoelectric effect; and incoherent (or Compton) scattering.[44] The likelihood of X-ray interaction can be subdivided into the sum of interaction probabilities from the three individual mechanisms. For convenience, it is helpful to consider and work with the mass

attenuation coefficient σ(E), (μ(E) normalized to density ρ) as it can be interpreted as a physical cross-section interaction probability or target size.

$$\frac{\mu(E)}{\rho} \equiv \sigma(E) = \sigma_R(E) + \sigma_C(E) + \sigma_\tau(E) \qquad [4].$$

In equation 4, the subscripts σ_R denote Coherent scattering, σ_C Compton scattering, and σ_τ the photoelectric effect.

Coherent scattering is unique from the other two forms of attenuation in that no energy from the interaction of the X-ray to the medium is deposited. Instead, a complex interaction with the energy lattice of molecular bonds occurs and causes a change in the X-ray trajectory, which is strongly forward peaked (i.e. undergoes a small change in angle). This type of interaction is more favorable at high atomic numbers and energies. The contribution of coherent scatter is proportional to Z^3/E (see **Figure 1-2**).

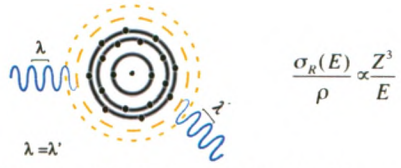

Figure 1-2. *Coherent (Rayleigh) scattering of X rays seen here only undergoes a change in direction from the initial trajectory and departs no energy to the atom.*

In the photoelectric effect, an X ray photon is completely absorbed by a bounded electron, which is ejected with an energy equal to the kinetic energy of the initial X ray photon minus the work potential to release the electron. Electron transitions from outer orbital shells will fill the void of the ejected electron and emit

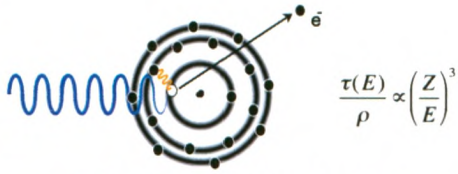

Figure 1-3. *The photoelectric effect occurs when photons of a sufficient energy can liberate bound electrons greater than their work potential. Cascading photons may be re-emitted in any direction from Auger electrons filling voids.*

characteristic radiation of that atom in the process. Occasionally though, and in particular with low atomic number atoms, no characteristic photon will be released, instead energy available from the cascading electron will be transferred to an orbiting electron and injected. The interaction likelihood for the photoelectric effect type in a material is peaked just above major atomic binding shell energies, but generally contributes to the total attenuation proportional to $(Z/E)^3$ (see **Figure 1-3**).

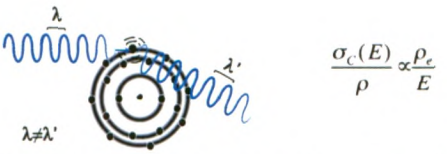

Figure 1-4. *The Compton effect occurs in an inelastic collision of x-ray photons with atomic electrons in which, some but never all of the photon energy is deposited to the recoiling electron.*

Incoherent or Compton scattering can be described as similar to the kinetics of billiard ball interactions. At higher energies (typically greater than the binding energies of the atomic electrons) X rays interact with the outer shell electrons and will deposit some, but never all, of their energy to the electron as seen in **Figure 1-4**. The likelihood of this interaction in a material is strongly dependent on density or more specifically electron density and therefore proportional to ρ_e/E.

An example of the fractional contributions of each type of interaction, as demonstrated with water, is shown in **Figure 1-5**. Often attenuation is assumed to result only from the photoelectric effect and Compton scattering, given that they dominate the majority of X ray attenuation in the diagnostically relevant zone.

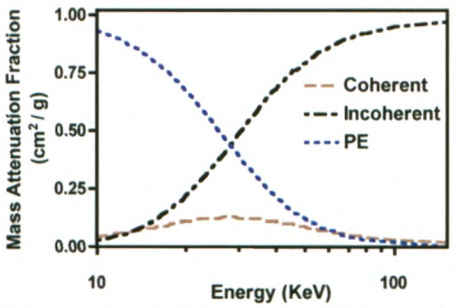

Figure 1-5. *Fractional contribution of the respective attenuation processes to the overall attenuation of X rays.*

The corresponding linear attenuation coefficients (μ) for water and some tissues, representing the total attenuation from all attenuation mechanisms, is shown in **Figure 1-6**.

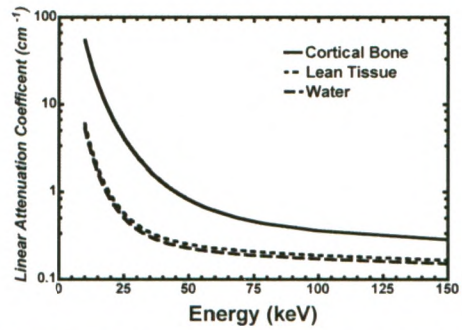

Figure 1-6. *The linear attenuation coefficients for water, cortical bone, and lean tissue.*

Dual-energy methods that decompose CT data to obtain essentially complete energy-dependent information (as in composition and density), are optimized for the acquisition of two to acquire two attenuation measurements—one primarily in the low (~40 KeV) photoelectric energy regime (corresponding to atomic number), and the second primarily in the higher (~100 KeV) Compton energy regime (corresponding to electron density).

1.3.3 X-ray Generation

Unfortunately, unlike common light emitting diodes, the band-gap required for X ray production is far too large, hindering the development of a simple solid-state device for X ray production. As a result, the process by which X rays are created is an energy inefficient procedure. X rays can be generated by synchrotrons,[45] or by free electron lasers,[46] but because these methods require significant

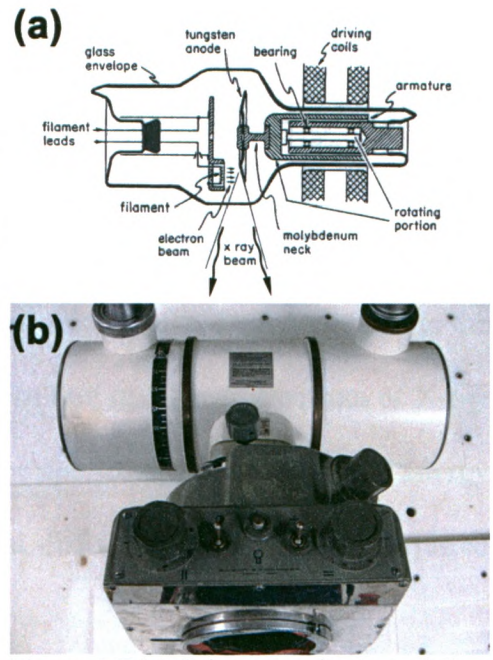

Figure 1-7.(a) *Schematic of a typical X-ray tube. (b) Photograph of an X-ray tube principally used in CT-based applications.*

infrastructure, it precludes their use in hospitals. Therefore, the vast majority of diagnostic X ray production results from compact X ray tubes. A schematic drawing and photograph of a typical X ray tube is shown in **Figure 1-7**.

One mechanism in which X-ray tubes generate X rays is a process referred to as *Bremsstrahlung* radiation, translated as "breaking radiation." In this method, charged particles (electrons) are accelerated across a strong potential toward an electrode and are slowed by the Coulomb field of the atoms in the electrode, emitting X-rays as they decelerate. According to classical theory, the total intensity of radiation produced from impinging particles of mass (m), and charge (*ze*) hitting a target composed of atoms having a charge (*Ze*) is proportional to:

$$I_{Bremsstrahlung} \propto \frac{Z^2 z^4 e^6}{m^2} \qquad [5].$$

Equation 5, indicates that greater radiation intensity will occur for a high Z target electrode and a favorable charge-to-mass ratio, like an electron. Since this process is highly inefficient at producing X rays (<1% energy output), a great deal of energy is released as heat, requiring the target material to be high in heat conductivity and have a high melting point, like tungsten. Depending on the proximity of a grazing electron to the atomic nuclei, the rate of deceleration will differ, resulting in a linear spectrum of X-ray energies, having a maximum energy equivalent to the applied potential difference energy (kVp). In typical X-ray tubes, the applied potential difference can usually be adjusted from 50 kVp to 120 kVp.

Additionally, accelerated charged particles will also be slowed by colliding and releasing atomic electrons, emitting characteristic radiation in the process. Because *bremsstrahlung* and characteristic radiation are produced at some depth level within the target anode, the primary X ray beam undergoes a small amount of filtration, resulting in lower-energy X rays preferentially being removed from the spectrum. A typical X-ray spectrum from an X ray tube is shown in **Figure 1-8**.

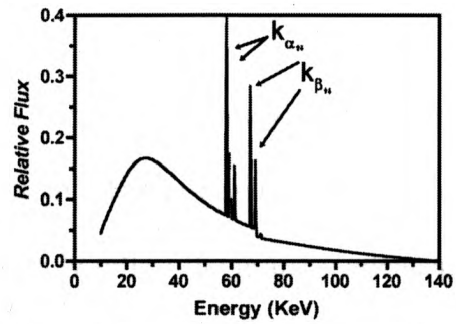

Figure 1-8. *Typical X ray spectrum from a CT-based X-ray tube, operating at 140 kVp.*

1.3.4 2-D to 3-D Image Reconstruction

The mathematical basis of generating a representative 3-D image volume from a series of its 2-D projection data was first proposed as early as 1917 by Johann Radon, who first applied this technique to problems involving gravity. Today there are two major approaches by which 2-D projection images are converted into a 3-D CT image volume, a filtered back-projection approach or an iterative approach,[47] the later of which is a computationally intensive method. The filtered back-projection method has been adapted for fan-and cone-beam X ray source-to-detector geometries, in which an approximate solution has proven useful for faster acquisition times. [48]

1.3.5 Micro-CT Summary

In summary, micro-CT systems use X rays to form 3-D images of the linear attenuation coefficients of objects, or small animals from 2-D transmission measurements (projections). The linear transmission coefficients mainly reflect the primary attenuation of X rays by the photoelectric and Compton processes, which differ for different materials and at different energies. CT systems use X rays with a broad spectrum of energies to form images. Typical CT devices can adjust the available X rays energies by altering the x-tube potential (kVp). Dual-energy or *K*-edge imaging techniques can therefore be implemented as simply as adjusting the kVp, and acquiring image data at more than one energy.

1.4 Micro-CT: Current Technology

Micro-CT imaging systems are now commercially available from all the major manufacturers of clinical CT scanners, such as General Electric, Siemens, and Phillips, in a variety of source-to-detector acquisition configurations. The two main configurations are distinguished as either *in vitro* specimen, or *in vivo* small animal scanners, as shown in **Figure 1-9**. The nominal resolution of micro-CT systems, (which depends to the first order on: X-ray focal size, the detector resolution, and geometric magnification) have been developed and reported in specimen scanners as fine as 6 μm.[49] At these resolutions, micro-CT has been shown to be complimentary to histological measurements.[28]

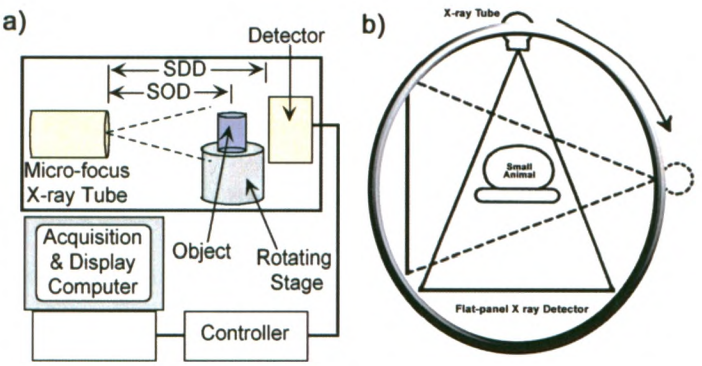

Figure 1-9. *The two main configurations of micro-CT scanner; (a) an in vitro specimen scanner and (b) an in vivo small animal scanner. Image (a) reproduced from Ford, Med. Phys.30(11) pp. 2869-77 (2003)*

Most commercially available micro-CT devices use image-intensifiers (to convert X ray photons into light) coupled to fiber-optic tapers; the visible light is then detected by a smaller charge-coupled device (CCD). A pitfall of this approach is a decreased light collecting ability, largely due to the packing fraction and numerical aperture of the circular optical fibres. However, recent advances in micro-CT technology include the use of high-resolution indirect X-ray converters, such as a cesium iodide (Thallium doped) flat-panel detector array, coupled to a thin-film transistor.[50] Modern flat-panel detectors for small animal imaging have been reported with large detector areas (1024x1024 pixels). An increasing number of X-ray systems are incorporating flat-panel detectors due to their fast digital readouts and higher dynamic range.[51]

Slip-ring technology was developed to allow the continuous rotation of the gantry around a patient in spiral clinical CT scanners, and has recently been incorporated into *in vivo* small animal scanners. The fast digital readouts from flat-panel detectors combined with slip-ring technology has resulted, in dynamic micro-CT, with full 3-D image volumes obtained at intervals of less than a second. In the course of a several-second

window, CT scanners operating in this fashion will obtain several image volumes that can be used to investigate the physiological function of small animals. [52]

The recent expansion of micro-CT to acquire dynamic data, to reveal physiological function, such as blood-flow rate, or visibly monitoring cardiac arrhythmia, does not overshadow the technology's proven ability to provide highly detailed 3-D anatomical data. Because of dramatic increases in computer processing speed and the abundance of computer memory, fast micro-CT acquisition systems are now used frequently as a tool for high-throughput characterizations of phenotypic expressions in small animals.[53]

1.5 Thesis Proposal

Quantitative evaluations of CT data – like material decomposition techniques – are still in their infancy. The transition from mostly qualitative techniques used by clinicians to quantitative analysis will likely improve and extend the efficacy of CT-based applications. Pre-clinical micro-CT studies will likely precede the majority of clinical applications using quantitative imaging techniques, especially in small animal applications. This thesis will demonstrate two analytical techniques for material-selective imaging in small animal micro-CT studies.

Using a newly developed dynamic flat-panel cone-beam micro-CT scanner CT (GE explore Locus Ultra, GE Healthcare, London, ON), we propose to decompose single-energy micro-CT data of whole rat specimens into adipose tissue, lean tissue and bone (inorganic and organic components). Furthermore, we will quantify by way of repeated measurements, the precision of the aforementioned micro-CT scanner to

characterize tissue using threshold techniques and typical scanning parameters. Using predetermined densities of adipose tissue, lean tissue and skeletal densities in rats, we will compare the total calculated weights of rats to the measured weights from a digital scale prior to imaging.

In the second objective, the same micro-CT scanner will be used to acquire dual- and triple-energy X ray attenuation measurements of rats perfused with Microfil MV-122. The post-reconstructed micro-CT data will then be processed with the specific intent to independently segment soft-tissue, bone and contrast-enhanced vessel. Decomposing micro-CT data into Microfil-perfused vessels and bone, should help to visualize vessels near bone where CT values, determined by *single-energy* CT, were too similar to distinguish by grey-scale alone.

1.6 Thesis Outline

This thesis is written in an integrated manuscript style, where chapter 2 and chapter 3 are intended for publication. Section 1.2 examines the current capabilities and applications of micro-CT and that are demonstrated in chapter 2. Section 1.3 lays the foundation for the physical basis for X-ray imaging in micro-CT and how it is technically achieved. The later section of 1.3 will provide the motivation to extend current capabilities of micro-CT by performing dual-energy and *K*-edge imaging, which forms the basis for chapter 3. Chapter 4 is a summary of the work presented and future applications for dual-energy and *K*-edge imaging.

1.7 References

1 M. D. Lairmore, L. Silverman, and L. Ratner, "Animal models for human T-lymphotropic virus type 1 (HTLV-1) infection and transformation", Oncogene **24**, 6005-6015 (2005).

2 E. Matteucci and O. Giampietro, "Proposal open for discussion: defining agreed diagnostic procedures in experimental diabetes research", J Ethnopharmacol **115**, 163-172 (2008).

3 Sir Patrick Bateson, "The use of non-human animals in research: a guide for scientists", (2004).

4 R. Weissleder, "Scaling down imaging: molecular mapping of cancer in mice", Nat Rev Cancer **2**, 11-18 (2002).

5 V. Koo, P. W. Hamilton, and K. Williamson, "Non-invasive in vivo imaging in small animal research", Cell Oncol **28**, 127-139 (2006).

6 J. S. Lewis, S. Achilefu, J. R. Garbow, R. Laforest, and M. J. Welch, "Small animal imaging. current technology and perspectives for oncological imaging", Eur J Cancer **38**, 2173-2188 (2002).

7 N. Beckmann, R. Kneuer, H. U. Gremlich, H. Karmouty-Quintana, F. X. Ble, and M. Muller, "In vivo mouse imaging and spectroscopy in drug discovery", NMR Biomed **20**, 154-185 (2007).

8 M. J. Paulus, S. S. Gleason, M. E. Easterly, and C. J. Foltz, "A review of high-resolution X-ray computed tomography and other imaging modalities for small animal research", Lab Anim (NY) **30**, 36-45 (2001).

9 T. F. Budinger, D. A. Benaron, and A. P. Koretsky, "Imaging transgenic animals", Annu Rev Biomed Eng **1**, 611-648 (1999).

10 M. R. Irwin, D. B. Downey, L. Gardi, and A. Fenster, "Registered 3-D ultrasound and digital stereotactic mammography for breast biopsy guidance", IEEE Trans Med Imaging **27**, 391-401 (2008).

11 M. Horger and R. Bares, "The role of single-photon emission computed tomography/computed tomography in benign and malignant bone disease", Semin Nucl Med **36**, 286-294 (2006).

12 D. W. Holdsworth, "Micro-CT in small animal and specimen imaging", Trends in Biotechnology **20**, S34-S39 (2002).

13 M. J. Paulus, S. S. Gleason, S. J. Kennel, P. R. Hunsicker, and D. K. Johnson, "High resolution X-ray computed tomography: an emerging tool for small animal cancer research", Neoplasia **2**, 62-70 (2000).

14 T. C. Lee, S. Mohsin, D. Taylor, R. Parkesh, T. Gunnlaugsson, F. J. O'Brien, M. Giehl, and W. Gowin, "Detecting microdamage in bone", J Anat **203**, 161-172 (2003).

15 J. L. Kuhn, S. A. Goldstein, L. A. Feldkamp, R. W. Goulet, and G. Jesion, "Evaluation of a microcomputed tomography system to study trabecular bone structure", J Orthop Res **8**, 833-842 (1990).

16 E. L. Ritman, "Micro-computed tomography of the lungs and pulmonary-vascular system", Proc Am Thorac Soc **2**, 477-480, 501 (2005).

17 W. W. Lam, D. W. Holdsworth, L. Y. Du, M. Drangova, D. G. McCormack, and G. E. Santyr, "Micro-CT imaging of rat lung ventilation using continuous image acquisition during xenon gas contrast enhancement", J Appl Physiol **103**, 1848-1856 (2007).

18 R. Ross, L. Leger, R. Guardo, J. De Guise, and B. G. Pike, "Adipose tissue volume measured by magnetic resonance imaging and computerized tomography in rats", J Appl Physiol **70**, 2164-2172 (1991).

19 S. Herman, "Computed tomography contrast enhancement principles and the use of high-concentration contrast media", J Comput Assist Tomogr **28 Suppl 1**, S7-11 (2004).

20 D. J. Kim, T. H. Kim, S. J. Kim, D. P. Kim, C. S. Oh, Y. H. Ryu, Y. J. Kim, and B. W. Choi, "Saline flush effect for enhancement of aorta and coronary arteries at multidetector CT coronary angiography", Radiology **246**, 110-115 (2008).

21 A. Goodman, L. Bornstein, H. Ball, D. M. Smith, and M. Bankoff, "Chromic phosphate therapy in carcinoma of the ovary", J Am Coll Surg **179**, 401-406 (1994).

22 O. Catalano, "[Computerized tomography in the study of acute sigmoid diverticulosis]", Radiol Med (Torino) **92**, 588-593 (1996).

23 D. A. Bakan, J. P. Weichert, M. A. Longino, and R. E. Counsell, "Polyiodinated triglyceride lipid emulsions for use as hepatoselective contrast agents in CT: effects of physicochemical properties on biodistribution and imaging profiles", Invest Radiol **35**, 158-169 (2000).

24 C. T. Badea, L. W. Hedlund, M. De Lin, J. F. Boslego Mackel, and G. A. Johnson, "Tumor imaging in small animals with a combined micro-CT/micro-DSA system using iodinated conventional and blood pool contrast agents", Contrast Media Mol Imaging **1**, 153-164 (2006).

25 L. O. Lerman, M. Rodriguez-Porcel, and J. C. Romero, "The development of x-ray imaging to study renal function", Kidney Int **55**, 400-416 (1999).

26 S. R. Walsh, T. Tang, M. E. Gaunt, and J. R. Boyle, "Contrast-induced nephropathy", J Endovasc Ther **14**, 92-100 (2007).

27 N. R. Powe, R. D. Moore, and E. P. Steinberg, "Adverse reactions to contrast media: factors that determine the cost of treatment", AJR Am J Roentgenol **161**, 1089-1095 (1993).

28 E. L. Ritman, "Molecular imaging in small animals--roles for micro-CT", J Cell Biochem Suppl **39**, 116-124 (2002).

29 M. Marxen, M. M. Thornton, C. B. Chiarot, G. Klement, J. Koprivnikar, J. G. Sled, and R. M. Henkelman, "MicroCT scanner performance and considerations for vascular specimen imaging", Med Phys **31**, 305-313 (2004).

30 R. E. Alvarez and A. Macovski, "Energy-selective reconstructions in X-ray computerized tomography", Phys Med Biol **21**, 733-744 (1976).

31 Philip Engler and William D. Friedman, "Review of dual-energy computed tomography techniques", Materials Evaluation **48**, 623-629 (1990).

[32] M. Moreau, D. W. Holdsworth, and A. Fenster, "Dual-energy x-ray imaging technique for in vitro tissue composition measurement", Med Phys **21**, 1807-1815 (1994).

[33] W. Kalender, W. Bautz, D. Felsenberg, C. Suss, and E. Klotz, "[Material-selective imaging and density measurement using the dual-energy method. I. Principles and methodology]", Digitale Bilddiagn **7**, 66-72 (1987).

[34] E. Roessl and R. Proksa, "K-edge imaging in x-ray computed tomography using multi-bin photon counting detectors", Phys Med Biol **52**, 4679-4696 (2007).

[35] S. J. Riederer, R. A. Kruger, C. A. Mistretta, D. L. Ergun, and C. G. Shaw, "Three-beam K-edge imaging of iodine using differences between fluoroscopic video images: experimental results", Med Phys **8**, 480-487 (1981).

[36] A. Sarnelli, H. Elleaume, A. Taibi, M. Gambaccini, and A. Bravin, "K-edge digital subtraction imaging with dichromatic x-ray sources: SNR and dose studies", Phys Med Biol **51**, 4311-4328 (2006).

[37] R. A. Kruger, S. J. Riederer, and C. A. Mistretta, "Relative properties of tomography, K-edge imaging, and K-edge tomography", Med Phys **4**, 244-249 (1977).

[38] S. J. Riederer and C. A. Mistretta, "Selective iodine imaging using K-edge energies in computerized x-ray tomography", Med Phys **4**, 474-481 (1977).

[39] P. Sukovic and N. H. Clinthorne, "Penalized weighted least-squares image reconstruction for dual energy X-ray transmission tomography", IEEE Trans Med Imaging **19**, 1075-1081 (2000).

[40] T. R. Johnson, B. Krauss, M. Sedlmair, M. Grasruck, H. Bruder, D. Morhard, C. Fink, S. Weckbach, M. Lenhard, B. Schmidt, T. Flohr, M. F. Reiser, and C. R. Becker, "Material differentiation by dual energy CT: initial experience", Eur Radiol **17**, 1510-1517 (2007).

[41] A. Garcia-Sanz, A. Rodriguez-Barbero, M. D. Bentley, E. L. Ritman, and J. C. Romero, "Three-dimensional microcomputed tomography of renal vasculature in rats", Hypertension **31**, 440-444 (1998).

[42] J. T. Butcher, D. Sedmera, R. E. Guldberg, and R. R. Markwald, "Quantitative volumetric analysis of cardiac morphogenesis assessed through micro-computed tomography", Dev Dyn **236**, 802-809 (2007).

[43] B. Rutt and A. Fenster, "Split-filter computed tomography: a simple technique for dual energy scanning", J Comput Assist Tomogr **4**, 501-509 (1980).

[44] Frank Herbert Attix, *Introduction To Radiological Physics And Dosimetry.* (Wiley-VCH, 2004).

[45] F. A. Dilmanian, "Computed tomography with monochromatic x rays", Am J Physiol Imaging **7**, 175-193 (1992).

[46] Claudio Pellegrini and Joachim Stohr, "X-ray free-electron lasers - Principles, properties and applications", Nuclear Instruments and Methods in Physics Research, Section A: Accelerators, Spectrometers, Detectors and Associated Equipment **500**, 33-40 (2003).

[47] T. Ziegler A Fau - Kohler, R. Kohler T Fau - Proksa, and R. Proksa, "Noise and resolution in images reconstructed with FBP and OSC algorithms for CT".

[48] L. A. Feldkamp, L. C. Davis, and J.W. Kress, "Practical cone-beam algorithm", Opt. Sci. Am. A. **1**, 612-619 (1984).

[49] M. D. Bentley, S. M. Jorgensen, L. O. Lerman, E. L. Ritman, and J. C. Romero, "Visualization of three-dimensional nephron structure with microcomputed tomography", Anat Rec (Hoboken) **290**, 277-283 (2007).

[50] A. L. Goertzen, V. Nagarkar, R. A. Street, M. J. Paulus, J. M. Boone, and S. R. Cherry, "A comparison of x-ray detectors for mouse CT imaging", Phys Med Biol **49**, 5251-5265 (2004).

[51] W. A. Kalender and Y. Kyriakou, "Flat-detector computed tomography (FD-CT)", Eur Radiol **17**, 2767-2779 (2007).

[52] L. Y. Du, J. Umoh, H. N. Nikolov, S. I. Pollmann, T. Y. Lee, and D. W. Holdsworth, "A quality assurance phantom for the performance evaluation of volumetric micro-CT systems", Phys Med Biol **52**, 7087-7108 (2007).

[53] T. Kohler, M. Stauber, L. R. Donahue, and R. Muller, "Automated compartmental analysis for high-throughput skeletal phenotyping in femora of genetic mouse models", Bone **41**, 659-667 (2007).

Chapter 2: Rapid *In Vivo* Whole-body Composition Of Rats From Cone-Beam Micro-CT

2.1 Introduction

Numerous epidemiological studies have shown that a disproportionately high percentage of adipose tissue (AT, or body fat) to total body weight (BW) has a direct correlation to a host of health-related problems in humans and animals.[1-4] Therefore, it is important to accurately measure and quantify, *in vivo*, the volume fraction of the three major weight contributors – adipose tissue, lean tissue (muscle), and bone – in the total body weight of mammals. Furthermore, any technique used to measure these quantities must be sufficiently precise enough, so that minute changes in the fractional proportion of the tissue volumes can be observed and monitored in longitudinal small animal studies. Many techniques have previously been developed to measure fractional tissue compositions in humans and in small animals, but most are either poor indirect measurements or invasive and destructive methods.[5-7]

Indirect techniques, though easily repeatable, make assumptions and approximations that can bias the true ratios of adipose tissue (AT), lean tissue (LT), and bone in total body composition.[8] This includes methods such as underwater weighing and body buoyancy or displacement measurements which rely on the assumption that the respective densities of AT and lean tissue remain constant.[6] Other indirect techniques

may use rudimentary anthropometric methods such as skinfold thickness or waist-to-hip ratio to infer body composition.[5]

The most direct and accurate method for obtaining body composition is chemical analysis, but this is highly destructive, precluding its use in longitudinal studies of animal specimens. Non-invasive *in vivo* imaging techniques, such as computed tomography (CT) and magnetic resonance imaging (MRI) have been shown to accurately quantify adipose tissue and lean tissue.[8] However, MRI imaging techniques, which use hydrogen (found mainly in water molecules) to form 3-D volumetric images *in vivo*, suffer in water-depleted regions, such as bone.

CT has been shown to be a highly accurate method for calculating tissue volumes and bone mineral content (BMC), based on image intensity alone, provided the tissues are sufficiently different in linear attenuation coefficients with respect to image noise.[8,9] Recently a high-throughput cone-beam micro-CT scanner (eXplore locus, GE Healthcare, London, On, Canada) has been developed that can acquire high resolution, 3-D volumetric images in acquisition intervals on the order of seconds. The nominal resolution offered by this micro-CT scanner (154 μm isotropic voxel spacing)[10] versus clinical scanners (nominal 600 μm), provides voxel sizes small enough to sufficiently reduce partial volume averaging when calculating regional tissue volumes based on thresholds, in micro-CT images of small animals.

In this chapter, we present micro-CT images of both *in vivo* and *ex vivo* whole-body rats that are post-processed to derive the total volume of adipose tissue, lean tissue,

and bone, based on single-energy CT image intensity. Voxels labeled as bone are additionally used to calculate the whole-body BMC for each rat. In order to calculate the precision of the cone-beam micro-CT imaging system to report BMC calculations, a subset of the rats will be imaged multiple times, post-mortem.

Furthermore, by imaging whole rat specimens and segmenting the images into volumes of adipose tissue (fat), lean tissue, and bone based on grey-scale intensity, we will calculate the cumulative weight of the respective volumes from average tissue densities reported in literature. Once the cumulative weights have been tabulated, we will compare the combined total calculated weight with the empirically measured weight of the specimen at the time of imaging. A final comparison will look at a previous study of similar rat specimens whose whole-body composition was measured by the gold standard chemical analysis.[11]

2.2 Methods

2.2.1 Micro-CT Imaging

A total of 25 dead female and 52 live male Sprague-Dawley rats, ranging in weights between 300-600 grams, were scanned using a cone-beam micro-CT volumetric scanner (GE eXplore Locus Ultra, GE Healthcare, London, ON). At the time of imaging, rats were placed on a digital balance and the weights were recorded. Scans were acquired using a 16-second, 1000 view protocol with an approximate transverse field of view (FOV) of 15.4 cm x 15.4 cm and longitudinal extent of 10.2 cm. X-rays were generated

using an x-ray tube potential of 120 kVp, a current of 20 mA, and no added filtration. Because the length of each rat was greater than the longitudinal extent of the FOV, three image volumes were acquired, each longitudinally displaced by 90 mm from the previous scan, in order to cover the entire rat contiguously from head to tail; a total length of 27 cm.

To assess the precision of our BMC measurements, a subset of six animals were imaged repeatedly, post-mortem. In this study, each animal was imaged 6 times (with repositioning), for a total of 36 whole-body scans and 108 image volumes (i.e. 3 sections x 6 rats x 6 repeated measurements = 108 acquired volumes). It has been calculated previously by Gluer *et al.* that 6 repeated measurements of bone mineral density (equivalently BMC) on 6 different subjects will result in a 95% confidence in a calculated precision value.[12]

Included in each scan were several cylindrical plugs containing a range of bone mineral equivalent densities. The first cylinder containing a tissue-equivalent plastic with zero bone mineral content, while at the other end of the range we included an epoxy cortical bone-mimicking calibrator (SB3, Gamex RMI, Middleton, WI)[13] having a bone mineral equivalent of 1100 mg/cc. A water phantom was also included in each image, to ensure accurate conversion of CT grey-scale intensities to Hounsfeld Units (HU) in each imaged volume.

The total dose to the live rats, consisting of three scans each at 120 kVp (20 mA, 16 sec.), was measured from x-ray exposure measurements. To obtain the exposure measurements, the gantry of the scanner was held fixed and a paddle ionization chamber

(model 96035, Keithley, Cleveland, OH) was placed in the centre of the field of view, perpendicular to, and completely within the x-ray beam. The paddle ionization chamber was connected to a dosimeter (model 35617, Keithley, Cleveland, OH) and the electrical charge (in nC) was recorded by the ion chamber for a 1.1 sec. exposure at 90 mA, 120 kVp. Measurement exposure (per mAs) in Roentgens was obtained using the model-specific ion-chamber conversion factor of 0.2327 R/nC and dividing by the exposure mAs. The total absorbed dose (in air), was then calculated using a conversion factor of $D_{air} = 0.876$ cGy R^{-1} for a single scan and a total of three combined scans.[14]

Images were reconstructed using the Feldkamp back-projection cone-beam algorithm at twice the detector pixel spacing, resulting in an isotropic voxel spacing of 308μm.[15] The three acquired volumetric images were cropped (to remove conebeam-related boundary artefacts) and digitally stitched together to produce a complete reconstructed volumetric image of the entire rat, having a total image size of 486 x 160 x 880 voxels in axial planes x, y and z, respectively. All reconstructed images were analyzed or processed with custom application software developed in c ++.

2.2.2 Calculation Of Adipose And Lean Tissue Volumes

For each reconstructed volume containing a whole rat specimen, a total of three global thresholds were used to label CT voxels as either adipose tissue, lean tissue or bone. The three thresholds were chosen based on the averaged histogram values observed in of 6 of the post mortem rats; within these histograms, two peaks were identified: one as AT, and the other as LT. Two Gaussian distributions were fit to the histogram, one to the AT peak and the other to the LT peak. A threshold (CT_{AIR}) separating air and AT was

chosen at 3 Standard deviations below the AT peak, and another threshold (CT_{BONE}), separating lean tissue from bone, was chosen at 3 Standard deviations above the lean tissue peak. A third threshold ($CT_{AT/LT}$) was chosen to separate AT from LT based on a greyscale segmentation algorithm described by the Ostu.[16] The voxels labeled as either AT, LT, or bone from the calculated thresholds were then visually inspected to confirm that the appropriate voxels were correctly identified.

The adipose tissue volume (ATV) and lean tissue (LTV) were calculated as;

$$ATV = \Delta x^3 \cdot (\text{Total \# of voxels bounded by } CT_{AIR}, \text{ and } CT_{AT/LT}) \quad [cm^3] \quad [1a]$$

$$LTV = \Delta x^3 \cdot (\text{Total \# of voxels bounded by } CT_{AT/LT}, \text{ and } CT_{BONE}) \quad [cm^3] \quad [1b]$$

where Δx is the linear dimension of an isotropic voxel (i.e. 0.0308 cm in our study).

2.2.3 Calculation Of Bone Mineral Content And Bone Volume

Two cylindrical region-of-interests (ROIs) (approximately 1000 voxels or 30.0 mm^3) were placed within each image volume, one in the tissue-equivalent calibrator and the other in the SB3 calibrator. The average CT value within each calibrator was calculated and represented as CT_{TE} and CT_{SB3}. Voxels having intensities above the bone threshold (> CT_{BONE}) are summed to calculate a total whole-body BMC for all bone voxels (N_{bone}) as,

$$BMC = N_{bone} \times \Delta x^3 \left(\frac{1100}{CT_{SB3} - CT_{TE}} \right) \sum_{i=1}^{i=N_{bone}} \frac{(CT_i - CT_{TE})}{N_{bone}} \quad [mg] \quad [2]$$

where, 1100 is the known mineral value of SB3 in mg cm^{-3}.

In calculating a bone volume, voxels classified as *bone* are considered to consist of an inorganic component (hydroxyapatite) and an organic component (collagen and fluid). Even at an isotropic voxel spacing of 308 μm, image regions labeled as bone have a surface-to-volume voxel ratio greater than 1, causing partial volume averaging to occur; therefore, in order to counteract this effect in the total bone volume calculation, a weighting term is included as listed in the equation below.

The total bone volume (BV) is calculated as;

$$BV = \Delta x^3 \cdot (\text{Total \# of voxels above } CT_{BONE}) \times (CT_{mean}/CT_{SB3}) \quad [cm^3] \quad [3]$$

where, CT_{mean} is the average value of the voxels defined as bone.

2.2.4 Whole-Body Fractional Weight Comparison To Chemical Analysis

While it is beyond the scope of this study to perform destructive chemical analyses to determine the accuracy of our calculated tissue volumes from micro-CT images of rat specimens, we provide a comparison to a previous study by Cortright *et al.*, (using similar Sprague-Dawley rats that have been examined by chemical analysis). In the previous study, two groups of 15 animals were studied, of which 7 males and 8 females were sedentary bred (SED), and 7 males and 8 females were exposed to daily spontaneous exercise (DSE). Following a 9 week period, the two groups were killed and studied using chemical analysis to reveal total body water, protein, fat and ash. In order to relate these four components to our derived body composition components: LT, AT, and BMC, lean tissue was calculated as (body water + protein – ash), while AT was related to

fat, and bone (inorganic) to ash.[11] No comparison was made to our derived whole-body composition of bone (inorganic and organic) to the external study.

2.3 Results

2.3.1 Segmentation Thresholds

The three thresholds, CT_{AIR}, $CT_{AT/LT}$, and CT_{BONE} were chosen from averaged histogram attributes select in regions of interest (approximately 1500 voxels) containing visible portions of AT, LT, and bone from the first 6 dead female rats. A Gaussian distribution was fit to AT peak and a second Gaussian distribution to the LT peak from the averaged histogram. Otsu's method was used to calculate a threshold to separate the two Gaussian peaks. A lower threshold was established at 3 standard deviations below the first peak (found at -140 HU) and a second threshold established at 3 standard deviations greater than the second peak (found at 90 HU). The three thresholds were found to be: CT_{AIR} = -225 HU, $CT_{AT/LT}$ = -18 HU, and CT_{BONE} = 200 HU, as shown in Figure 1.1. These thresholds were also found to be suitable for the live rats and were used throughout the study for consistency. All images were inspected visually to confirm that the appropriate voxels were identified using the thresholds selected. An example image is shown in **Figure 2-2**.

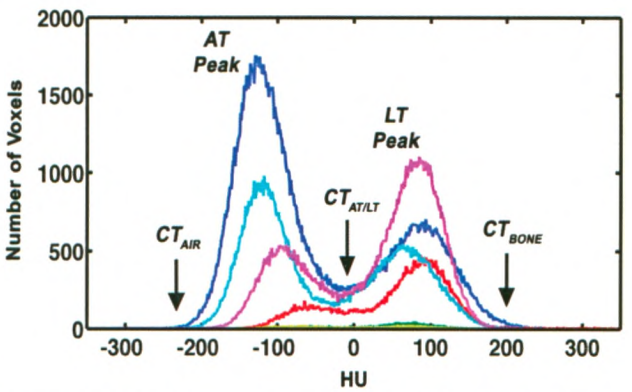

Figure 2-1 *Histogram from ROIs containing bone, fat, and lean tissue for each of the dead rats (1-6).*

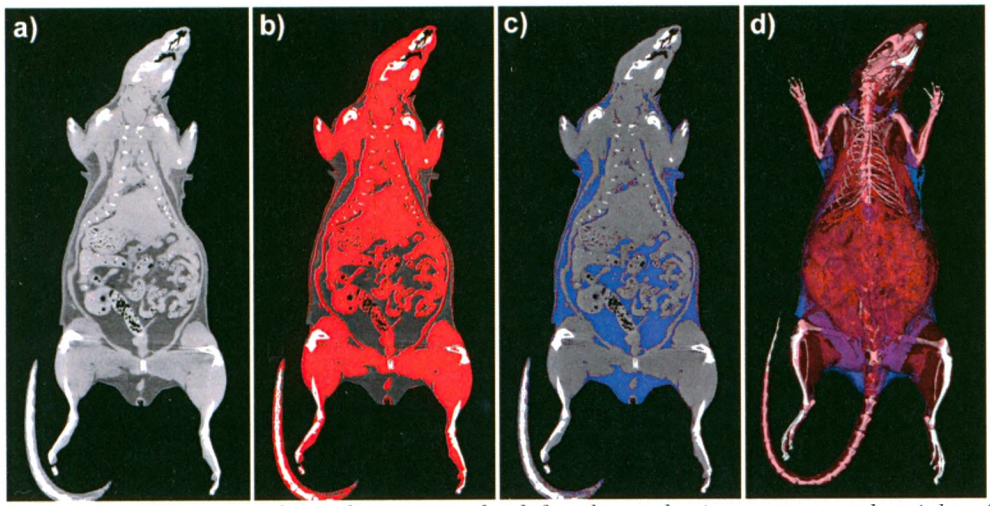

Figure 2-2 *CT image slice of an entire dead female rat having a measured weight of 338 grams. (a), the same rat decomposed into lean tissue (b), adipose tissue (c) and the combined lean tissue, adipose tissue and bone volumes, shown in a volume rendered image (d).*

2.3.2 Precision and Dose Tabulated

The total bone mineral content was measured and calculated 6 times for 6 different rats (dead female rats 1-6) based on the work of Gluer *et al.* to report confidence in the scanner's precision for this technique, with repositioning. The precision was calculated based on the root-mean-squared (RMS) average of the variances calculated for each rat's BMC measurements. The scanner's precision in the determination of bone mineral content was found to be ± 0.9%.

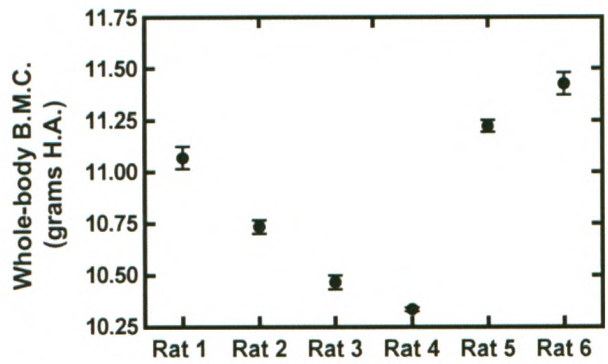

Figure 2-3 *Graph depicting the whole-body bone mineral content measured in post-mortem female rats (1-6). Error bars indicate the standard deviation in the 6 repeated measurements.*

The total whole-body dose was calculated to be 0.301 Gy (consisting of three 16-sec. scans, at 120 kVp, 20 mA) or 5.6 % of the reported LD50/30 for rats.[17]

2.3.3 Conversion Of Tissue Volumes Into Estimated Weight

The conversion of adipose tissue, lean tissue, and bone tissue volumes into weights was accomplished by multiplying each volume by the tissue densities reported in the literature, which are 0.95, 1.06, and 1.94 gcm^{-3}, respectively.[18] The average CT-derived tissue masses for the dead female and live male group were calculated and listed in **Table 2-1**. The cumulative tissue weights were also calculated and found to be 368.6 grams for the average of the dead female group of rats and 435.0 grams for the average of the live male group of rats. These values differed from the average gravimetrically measured group values by 5.4 and 0.2 %, respectively.

2.3.4 Fractional Whole-Body Mass Comparison To Chemical Analysis

While a comparison to a previously studied group of similar Sprague-Dawley rats under chemical analysis is anecdotal, the tissue masses were in the appropriate ranges as observed in **Table 2-1**.

Group	*n*		Adipose Tissue	Lean Tissue	Bone (Inorganic, i.e. BMC)	Bone (Inorganic and Organic)	Measured Weight	Calculated Weight	Percent Diff.
Female (dead)	25	*grams*	*60 ± 20*	*260.0 ± 20*	*10.3 ± 0.6*	*39 ± 2*	*350 ± 1*	*370 ± 40*	5
		%	**16 ± 6**	**71 ± 6**	**2.9 ± 0.2**	**10.0 ± 0.4**			
Male (living)	52	*grams*	*30 ± 20*	*350 ± 90*	*11 ± 8*	*49 ± 8*	*436 ± 1*	*440 ± 130*	0.2
		%	**8 ± 4**	**80 ± 20**	**2.7 ± 0.1**	**11.0 ± 2**			
***Female (SED)**	8	*grams*	*33 ± 3*	*250 ± 10*	*11.1 ± 0.3*		*302 ± 14.8*		
		%	**11 ± 1**	**83 ± 1**	**3.6 ± 0.1**				
***Male (SED)**	7	*grams*	*80 ± 5*	*460 ± 10*	*15.7 ± 0.6*		*548 ± 9.6*		
		%	**14.6 ± 0.8**	**84 ± 1**	**2.9 ± 0.1**				
***Female (DSE)**	8	*grams*	*24 ± 5*	*250 ± 10*	*11.3 ± 0.4*		297.0 ± 9.9		
		%	**8 ± 1**	**85 ± 4**	**3.8 ± 0.1**				
***Male (DSE)**	7	*grams*	*42 ± 7*	*430 ± 10*	*15.9 ± 0.5*		*498 ± 21*		
		%	**8.0 ± 1**	**87 ± 5**	**3.2 ± 0.1**				

Table 2-1 *The top two rows show the calculated tissue masses for the two groups of rats examined by micro-CT. The bottom 4 rows show 4 similar groups of rats of a previous study by Cortright et al., which calculated the tissue masses in male and female sedentary bread (SED) groups and in male and female daily spontaneous exercise (DSE) group by post-mortem chemical analysis.*

2.4 Discussion

We have successfully demonstrated that we can separate lean tissue, adipose tissue and bone, based on gray-scale intensities within single-energy micro-CT images alone, facilitating quantitative assessment of phenotype of laboratory rodents. By micro-CT imaging of whole rat specimens, we have calculated the total fractional composition of AT, LT, and bone. By selecting the appropriate densities for the tissues we were also able to calculate the total weight of each rat, based solely on radiographic data. Micro-CT images of whole-body 25 dead female and 52 live male rats were decomposed into their whole-body compositions and average total body weights for the groups calculated. The average calculated weight of the dead female group was found to be 5.4 % different than the empirically measured weight, while the average calculated weight of the live male group was found to be 0.2% different than the empirically measured weight. The

difference between the two groups may be partially due to the fact that the dead group was left in a plastic bag when scanned.

In addition, the total bone mineral content for each group of rats was calculated. The similarity of our BMC calculations to bone ash in the previous external study – investigating body composition of similar rats under chemical analysis – suggest that we achieved characteristic amounts of BMC and fraction tissue compositions. In addition, by repeated measurements of whole-body BMC, we have calculated the precision of the micro-CT system's ability to report BMC measurements at ± 0.9%, indicating that it is highly sensitive in monitoring changes in body composition.

We have also shown that whole-body micro-CT imaging of rats can be performed at an acceptable dose level of 0.3 Gy. This exposure to ionizing radiation should be safe for small-animal longitudinal studies, given that previous studies have indicated that the repair processes in rodents will allow mice (which are about 10 times smaller thans rats) to neutralize 0.25 Gy of radiation per day.[19]

2.5 Conclusion

In this study, we have shown that quantitative *single-energy* micro-CT data can be successfully separated into three tissue components in rodents, (i.e adipose, lean, and bone) under the following conditions:

1) The materials can be compartmentalized (i.e. not a miscible solution)

2) The materials can be identified in homogenous regions in the image that are relatively large in comparison to the reconstructed voxel size

3) The materials differ sufficiently different in linear attenuation coefficient, such that they can be separated successfully, even with random CT image noise.

In situations where a contrast-enhanced media is biologically introduced, and cannot be immediately removed, material decomposition using thresholds in *single-energy* micro-CT may fail. In this case, the classification scheme might fail to identify compartments (limitation 1) or (as is likely to be the case), the materials will be too similar in grey-scale intensity to be distinguishable (limitation 3). For example, a vascular contrast agent with signal intensity similar to bone and which remains in the vessels for an extended period of time (i.e. a blood-pool agent) will not be distinguished in regions where vessel meets bone, based on grey-scale thresholds alone. In the following chapter, I describe how this limitation can be overcome, through the use of dual-energy CT imaging.

2.6 Acknowledgements

I would like to thank Earl Noble, and Bruce Frier for the live group of rats, and Eva Turley for the group of post-mortem rats.

2.7 References

1 O. Lamas, A. Marti, and J. A. Martinez, "Obesity and immunocompetence", Eur J Clin Nutr **56 Suppl 3**, S42-45 (2002).

2 G. S. Young and J. B. Kirkland, "Rat models of caloric intake and activity: relationships to animal physiology and human health", Appl Physiol Nutr Metab **32**, 161-176 (2007).

3 P. W. Wilson, R. B. D'Agostino, L. Sullivan, H. Parise, and W. B. Kannel, "Overweight and obesity as determinants of cardiovascular risk: the Framingham experience", Arch Intern Med **162**, 1867-1872 (2002).

4 T. S. Han, M. A. Tijhuis, M. E. Lean, and J. C. Seidell, "Quality of life in relation to overweight and body fat distribution", Am J Public Health **88**, 1814-1820 (1998).

5 M. D. Jensen, "Research techniques for body composition assessment", J Am Diet Assoc **92**, 454-460 (1992).

6 J. Wang, S. B. Heymsfield, M. Aulet, J. C. Thornton, and R. N. Pierson, Jr., "Body fat from body density: underwater weighing vs. dual-photon absorptiometry", Am J Physiol Endocrinol Metab **256**, E829-834 (1989).

7 P. B. Johansen, A. Flyvbjerg, M. Wilken, and K. Malmlof, "Comparison of methods of analysis of body composition in hypophysectomized rats treated with rat growth hormone", Growth Horm IGF Res **10**, 342-348 (2000).

8 R. Ross, L. Leger, R. Guardo, J. De Guise, and B. G. Pike, "Adipose tissue volume measured by magnetic resonance imaging and computerized tomography in rats", J Appl Physiol **70**, 2164-2172 (1991).

9 P. Steiger, J. E. Block, S. Steiger, A. F. Heuck, A. Friedlander, B. Ettinger, S. T. Harris, C. C. Gluer, and H. K. Genant, "Spinal bone mineral density measured with quantitative CT: effect of region of interest, vertebral level, and technique", Radiology **175**, 537-543 (1990).

10 L. Y. Du, J. Umoh, H. N. Nikolov, S. I. Pollmann, T. Y. Lee, and D. W. Holdsworth, "A quality assurance phantom for the performance evaluation of volumetric micro-CT systems", Phys Med Biol **52**, 7087-7108 (2007).

11 R. N. Cortright, M. P. Chandler, P. W. Lemon, and S. E. DiCarlo, "Daily exercise reduces fat, protein and body mass in male but not female rats", Physiol Behav **62**, 105-111 (1997).

12 C. C. Gluer, G. Blake, Y. Lu, B. A. Blunt, M. Jergas, and H. K. Genant, "Accurate assessment of precision errors: how to measure the reproducibility of bone densitometry techniques", Osteoporos Int **5**, 262-270 (1995).

13 D. R. White, "Tissue substitutes in experimental radiation physics", Med Phys **5**, 467-479 (1978).

14 J. F. Valley and P. Lerch, "Letter: Dose conversion factors at the calibration beam energy", Phys Med Biol **18**, 744-746 (1973).

15 L.A. Feldkamp, L. C Davis, and J. W. Kress, "Practical cone-beam algorithm", Journal of the Optical Society of America A **1**, 612- (1984).

[16] Nobuyuki Otsu, "Threshold selection method from gray-level histograms", IEEE Transactions on Systems, Man and Cybernetics **SMC-9**, 62-66 (1979).

[17] H. I. Kohn, "Effect of immaturity, hypophysectomy and adrenalectomy upon changes in blood plasma of rat during acute radiation syndrome", Am J Physiol **165**, 43-56 (1951).

[18] M.J. Berger, J.H. Hubbell, S.M. Seltzer, J. Chang, Coursey J.S., R. Sukumar, and Zucker D.S., "National Institutes of Standards and Technology Photon Cross Sections Database " (1998).

[19] R. H. Mole, "Quantitative observations on recovery from whole body irradiation in mice. II. Recovery during and after daily irradiation", Br J Radiol **30**, 40-46 (1957).

Chapter 3: Dual- and Triple-Energy Cone-Beam Micro-CT Post-Reconstruction Material Decomposition

3.1 Introduction

The development of micro-CT has provided a powerful tool for small animal research models.[1-5] The high-resolution images achieved in micro-CT allow for quantitative in vivo and ex vivo analysis for such applications as: bone mineral measurements,[6,7] organ vasculature[8] and bone micro-architecture extraction.[9-11] Continued developments of exogenous contrast agents further extend the use of current micro-CT techniques, by highlighting physiological features not normally observed in tissue.[8,12-14] Despite advancements in contrast agents, a limitation of single-energy CT is that two different materials may share similar grey-scale intensity values, making it difficult to perform image segmentation based on grey-scale signal intensity alone.

Dual-energy computed tomography (DECT) has been shown to transform CT grey-scale intensity values into both effective atomic number and electron density, or into the relative abundances of three materials[15] and is recently gaining popularity in clinical applications with the introduction of dual-source CT scanners.[16] Most dual-energy CT techniques exploit the fact that one can represent the two dominant attenuation processes as a simple set of linear basis functions.[17-20] Alvarez and Macovski have derived functional relationships, applicable at diagnostic x-rays energies (approximately 20-to-150 keV), which can be used to solve for effective atomic number and electron density.[19]

One basis function relates the photoelectric effect to atomic number and another relates Compton scattering to electron density. Solutions to the basis functions are obtained by acquiring two attenuation measurements – one at an energy where the photoelectric effect dominates, and another at an energy dominated by Compton scattering. Using this technique, CT images are processed and interpreted to indicate both composition and density, on a voxel-by-voxel basis. Commonly, DECT is performed by preprocessing the raw projection data by using a priori knowledge of the spectra and attenuation coefficients of the constituent material,[18-22] but recently an empirical dual- energy calibration procedure was proposed based on the use of a calibration phantom to remove the need for a priori knowledge.[23]

Materials possessing atomic numbers greater than 40 exhibit sharp changes in x-ray attenuation due to the liberation of a *K*-shell electron in the diagnostic x-ray regime. For these materials, the presence of a *K* edge allows the decomposition of dual-energy CT images into material-specific images, where the intensities correspond to the relative abundances of the pre-defined basis materials.[15] Furthermore, the acquisition of a third energy may be added, resulting in a potential improvement in the accuracy of decomposition.[22,24,25] X-ray imaging using multiple energies sensitive to an element's *K* edge – a process referred to as *K*-edge imaging – has been explored in the past where efforts have focused on isolating iodinated contrast agent in fluoroscopic video images,[26] digital subtraction radiography,[27,28] and CT.[29-31]While iodinated contrast agents are routinely used for contrast-enhanced CT imaging,[32,33] pre-clinical micro-CT imaging techniques have additionally included the use of heavy elements,[2] such as a lead-based

media in *ex vivo* studies with small animals and tissue specimens.[8,34,35] In particular, the vascular contrast-casting agent Microfil (MV-122, Flow Tech, Carver, MA) can perfuse the microvasculature (vessels < 100 μm) of sacrificed animal specimens. [35] Microfil, a silicone-rubber compound containing lead, rapidly cures into a cast of a specimen's vasculature. Single-energy micro-CT images of perfused specimens can be used to provide quantitative measurements of vessels in organs, such as the heart,[36] kidney,[37] and prostate.[38] Unfortunately, at typical diagnostic energies, the CT number of Microfil in perfused specimens is close to that of cortical bone, [35,39] precluding the use of grey-scale segmentation to extract vessels near bone.

Incorporating DECT and *K*-edge imaging should improve the differentiation between vasculature (perfused with Microfil) and cortical bone, where they often appear too similar to isolate by grey-scale intensity alone. A dynamic volumetric cone-beam micro-CT system (GE explore Locus Ultra, GE Healthcare, London, ON), which has been used for a range of small-animal studies,[13,39-47] has the ability to acquire high-resolution images using energies above the *K* edge of lead, while handling greater power loads on the x-ray tube over a wider range of energies, making it suitable for the implementation of DECT and *K*-edge imaging of small animals.

We report dual- and triple-energy post-reconstruction techniques, implemented using a cone-beam micro-CT scanner, with the specific intent to independently segment bones and contrast-enhanced vessels in *ex vivo* studies with rodents. Numerical modeling of the x-ray spectra and image formation process was first used to determine the

acquisition energies for optimal material decomposition. The three optimized energy spectra were then used to acquire 3-D volume data sets, which were subsequently used to generate independent images of the three basis materials: cortical bone, contrast-enhanced vessel and soft tissue. The material decomposition techniques are investigated for both dual- and triple-energy acquisitions, with images obtained of a phantom and of a rat perfused with the exogenous lead-based contrast agent Microfil.

3.2 Theory

3.2.1 Approach To Material Decomposition

To decompose CT data into independent images of cortical bone, Microfil and soft tissue we applied the algorithm previously described by Vinegar and Wellington[48] for dual-energy imaging. Vinegar and Wellington proposed that two x-ray spectra with mean energies straddling the *K* edge of a doping agent (such as iodine) in oil would provide optimal material decomposition within geological core samples containing water, oil, and gas. In their implementation, Vinegar and Wellington were unable to achieve modified x-ray spectra to provide these mean energies, while simultaneously maintaining image quality, but were able to demonstrate that it is still possible to perform material decomposition using two polyenergetic spectra with widely separated mean energies.

In our study, to generate independent images of cortical bone, Microfil, and soft tissue, spectra containing different proportions of x rays with energies above the *K* edge of lead (88 KeV) are required. Below we briefly describe the dual-energy decomposition approach, as well as an extension to a triple-energy algorithm, which may improve the decomposition accuracy when three materials are present.

3.2.2 Dual-energy decomposition algorithm

As described by Vinegar and Wellington,[48] the mean attenuation coefficient (μ) measured in each volume element (voxel) of a CT image acquired with a mean energy E can be expressed as a linear combination of the attenuation coefficients of the basis materials multiplied by their volume fraction:

$$\mu_{CB,E} \cdot f_{CB} + \mu_{MF,E} \cdot f_{MF} + \mu_{ST,E} \cdot f_{ST,E} = \mu_E \quad . \qquad [1]$$

In Eq. (1) $\mu_{CB,E}$, $\mu_{MF,E}$, and $\mu_{ST,E}$ are the mean linear attenuation coefficients of cortical bone, Microfil, and soft tissue, respectively, and f_{CB}, f_{MF}, and f_{ST} represent the volume fractions of the three basis materials. If a voxel contains only three basis materials, the sum of the volume fractions must add to unity:

$$f_{CB} + f_{MF} + f_{ST} = 1 . \qquad [2a]$$

When two CT images are acquired with mean energies E1 and E2, two independent measurements are made of the attenuation coefficients as follows:

$$\mu_{CB,E1} \cdot f_{CB} + \mu_{MF,E1} \cdot f_{MF} + \mu_{ST,E1} \cdot f_{ST} = \mu_{E1} \qquad [2b]$$

$$\mu_{CB,E2} \cdot f_{CB} + \mu_{MF,E2} \cdot f_{MF} + \mu_{ST,E2} \cdot f_{ST} = \mu_{E2} \qquad [2c].$$

The linear attenuation coefficients for the basis materials μ_{MF}, μ_{CB}, and μ_{ST} at each energy can be measured from the CT images within regions known to contain the respective basis materials. (Note that in this application the mean attenuation coefficient and the CT number can be used interchangeably, because of the linear relationship between the two.) The solution for the three equations (2a, 2b, and 2c) having three unknowns (f_{CB}, f_{MF}, and f_{ST}) can be found using matrix factorization. With the additional *a priori* knowledge that the percentage concentration of each of the three basis materials

must be positive, a non-negative constraint must be placed on the matrix factorization. Lastly, note that voxels with CT numbers below soft tissue (i.e. air-containing regions) are excluded from processing and assumed to contain no basis materials.

3.2.3 Triple-energy decomposition algorithm

If an additional CT scan, acquired with a third mean energy (E3), is introduced in an attempt to improve the decomposition, the algorithm of Vinegar and Wellington[48] can be extended to include a third equation describing the mean attenuation coefficient (μ_{E3}) within a voxel:

$$\mu_{CB,E3} \cdot f_{CB} + \mu_{MF,E3} \cdot f_{MF} + \mu_{ST,E3} \cdot f_{ST} = \mu_{E3} \qquad [3].$$

The over-determined system of equations can be solved by computing and minimizing the mean squared difference (Δ) between the measured attenuation coefficients at each energy (μ_{E1}, μ_{E2}, and μ_{E3}) and calculated attenuation coefficients ($\mu_{Calc,E1}$, $\mu_{Calc,E2}$, $\mu_{Calc,E3}$) for all possible combinations of basis-material volume fractions:

$$\Delta\Big|_{f_{CB}, f_{MF}, f_{ST}} = \sum_{i=1}^{3} (\mu_{Calculated,Ei} - \mu_{Observed,Ei})^2. \qquad [4]$$

Equation (4) is calculated for all combinations of volume fractions f_{CB}, f_{MF}, and f_{ST}, at discrete intervals ranging between 0 and 1; i is an index used to identify the different energy spectra used. A grid search (also known as an exhaustive search) can then be performed to identify the minimum Δ, thereby identifying the volume fractions of each material in the voxel.[49]

3.3 Methods

3.3.1 Determination of Optimal X-ray Spectra

3.3.1.1 Selection of filtration

For the dual-energy approach implemented in this study we selected lead and copper as the materials used to filter the polyenergetic x-ray beam of the CT scanner. Lead filtration was added to sharply remove energies above the K edge of lead, while copper filtration was added to increase the mean energy of the high-energy spectrum to be as high as possible, while preserving adequate photon fluence.

Filter thicknesses were determined empirically by selecting the maximum available kVp on the CT scanner (140 kVp, see Section 3.3.3.3), and by setting the tube current to the maximum value determined by the x-ray tube cooling characteristics (100 mA for an 8 s. repeated scan). For both copper and lead, a filter thickness was selected to ensure that the full dynamic range of the detector was used (at the maximum current, without saturating the detector). Bright fields were acquired with varying thicknesses of copper or lead placed between the x-ray tube and detector; the filter thickness was reduced until blocks of pixels with identical values, indicating detector saturation, were observed in the acquired bright field. Ultimately, a copper filter thickness of 1.45 mm and a lead thickness of 0.3 mm were used. No filtration was added to the low-energy spectrum used in the triple-energy decomposition.

3.3.1.2 Modeling dual-energy decomposition

To determine the optimal x-ray tube potential energies to use in dual-energy decomposition, we modeled the x-ray spectral characteristics of the micro-CT scanner,

the interaction with the materials of interest (cortical bone, Microfil, and soft tissue) and the energy-weighted detector sensitivity. The simulation was implemented using Matlab (Version 7.1.0.183, The MathWorks Inc, Natick, MA USA).

X-ray spectra were simulated at 0.2 kVp increments, based on a semi-empirical model for a tungsten-target anode x-ray tube.[50,51] Scanner-specific parameters, such as target material composition (90% W, 10% Re), target angle (9°), distance from source-to-isocenter (54 cm), inherent beam filtration (0.15 mm Cu, 1.2 mm Al, and 2 mm Lexan) were included as input parameters. The response of the 0.42 mm thick Tl-doped, CsI scintillator (see Section 3.3.3.2) was modeled based on the previously reported energy-sensitive absorption efficiency and Swank factor for this scintilator.[52-54]

The linear attenuation coefficients of the basis components were also incorporated within the simulation. The chemical compositions of cortical bone and soft tissue were obtained from the ICRU report on tissue substitutes.[55] Because the composition of Microfil was unavailable, the chemical composition was estimated based on: information provided within the material safety data sheets, measurements of density and attenuation coefficients of the constituents shipped by the manufacturer, and comparison with similar silicone-rubber based compounds with known compositions. The composition of Microfil modeled in the numerical simulation is provided in **Table 3-1**. Based on these material compositions, the x-ray cross sections were obtained from the National Institute of Standards and Technology's online database[56] and used in the simulation.

Microfil component	MSDS	Compound	Molecular Formula	Contribution by Weight (%)
MV-122 Compound	Listed	Lead Sulfate	$PbSO_4$	4.48
	Listed	Lead Chromate	$PbCrO_4$	4.48
	Unlisted	Polymethylhydrogensiloxane (e.g. Dow Corning MH 1107)	$(CH_3)_6Si_2O(SiOCH_4)n$	39.3
MV Diluent	Unlisted	Dimethyl siloxane Polymer (e.g. Dow Corning 200 fluid)	$(C_2H_6OSi)n$	46.8
Curing Agent	Listed	Ethyl Silicate	$C_8H_{20}O_4Si$	1.95
	Listed	Dibutyltin Dilaurate	$C_{32}H_{64}O_4Sn$	2.93

Table 3-1 *The assumed composition of Microfil MV-122 silicone-rubber casting compound, used to calculate the effective linear attenuation coefficient in the numerical simulations.*

The effective linear attenuation coefficients for cortical bone, Microfil, and soft tissue were calculated for spectra with tube potentials ranging between 60 and 140 kVp, at 1 kVp intervals. For each tube potential, two protocols were simulated to incorporate the 0.3 mm Pb filtration (E1) and the 1.45-mm Cu filtration (E2). To identify the specific pair of x-ray spectra that optimize the difference between μ_{MF} and μ_{CB}, a novel figure of merit was defined, based on the report by Vinegar and Wellington.[48] Following this approach, the maximum separation between cortical bone and Microfil will be achieved when at E1 x rays are primarily attenuated by cortical bone and at E2 x rays are attenuated primarily by Microfil. Therefore, we defined a figure of merit – the cortical bone to Microfil contrast ratio (CMCR) – as follows:

$$CMCR = \frac{CT_{MF}^{E2} - CT_{ST}^{E2}}{CT_{CB}^{E2} - CT_{ST}^{E2}} \Big/ \frac{CT_{CB}^{E1} - CT_{ST}^{E1}}{CT_{MF}^{E1} - CT_{ST}^{E1}}. \qquad [5]$$

CMCR was calculated for the range of energies described above and the pair of spectra that maximized CMCR were identified and used in all experimental procedures.

3.3.2 Numerical simulation of dual- and triple-energy decomposition

The performance of the dual-energy and triple-energy decomposition algorithms was first evaluated using simulated CT images, to determine the effect of noise on the accuracy of material decomposition. Throughout this manuscript we use the term noise to refer to the standard deviation of a small region of interest defined in a uniform region of the image. Volumetric CT images (200×200×200 voxels) were simulated to represent images obtained at the three selected mean energies, listed in **Table 3-2**. The images consisted of three cylindrical vials (200-pixel depth, 40-pixel diameter – corresponding to 6-mm diameter objects at a pixel size of 150 μm), containing the three basis materials (cortical bone, Microfil, and soft tissue, as defined in section 3.3.1.2) surrounded by air. The grey-scale intensity of the air was set to -1000 HU, and the intensity of each cylinder was based on the calculated effective attenuation coefficient, represented in HU, for the material at each of the three mean energies. Images were simulated with no added noise and with the addition of Gaussian noise having standard deviations between 1 and 30 HU. Noise was added based on a random selection from a Gaussian distribution. [57]

Scan Protocol Number	Tube Potential (kVp)	Tube Current (mA)	Added Filtration (mm)	Mean Energy (KeV)
1 (E1)	96	160	0.3 Pb	68
2 (E2)	140	100	1.45 Cu	84
3 (E3)	70	190	0	49

Table 3-2 *Summary of scan protocols used for the dual- and triple-energy decomposition experiments. Protocols 1 and 2, used for dual-energy decomposition, were selected to maximize the difference in CT number between cortical bone and Microfil at the two mean energies.*

The dual- and triple-energy decomposition algorithms described in Sec. II.A were implemented using C++ and compiled using g++ (Version 4.0.2, Free Software Foundation, Boston, MA) for material decomposition of both the numerically simulated and experimentally acquired images. The grey-scale values within each material-specific image represented the percentage of material present within a voxel. To determine the accuracy of the decomposition algorithms, the mean and standard deviation of five regions of interest (1000 voxels each) randomly defined within each material "vial" were calculated. All image analysis was performed using Microview software (GE Healthcare, London, ON).

3.3.3 Experimental dual- and triple-energy decomposition

3.3.3.1 Phantom

A phantom containing Microfil, a cortical-bone-mimicking material (SB3, Gamex RMI, Middleton, WI) and acrylic (to mimic soft tissue) was manufactured. SB3 is an epoxy (CB2, 32.51 % by weight) containing calcium carbonate (67.49 % by weight) and has a density of 1.84 g/cm^3.[58] Inconsistencies in the homogeneity of SB3 and Microfil can occur, but can be identified by pre-scanning the SB3 material or reduced by careful preparation of Microfil. Cylindrical wells, 4 mm in diameter, were machined into a 26-

mm diameter acrylic cylinder; a 4-mm diameter plug of SB3 was inserted into one of the holes and Microfil (mixed 5 parts MV-122 to 4 parts diluent) was injected into a second well and allowed to cure. A third well, machined in the centre of the phantom, contained water, which was used to linearly rescale the image into CT values (in HU).

3.3.3.2 Micro-CT scanner and x-ray filtration

All images were acquired using the eXplore Locus Ultra cone-beam micro-CT scanner. The scanner uses a 1024×1024 matrix flat-panel detector,[40] with isotropic pixel spacing of 200 μm, and a clinical x-ray tube; the detector and x-ray tube are mounted on a slip-ring gantry that can rotate as fast as once per second. The x-ray tube (Solarix GS-3576S, Varian, Salt Lake City. UT) operates at tube potentials between 70 and 140 kVp, with a maximum power-loading limit of 21 kW; clinically, this tube is used for CT applications. A previous study has reported the imaging performance parameters for this cone-beam CT scanner,[39] including spatial resolution, linearity, geometric accuracy, uniformity, and noise. The modulation transfer function reached a value of 10% at 2.5 mm^{-1} (corresponding to an effective spatial resolution of 200 μm) at typical noise levels of about 25 HU for a 1200 mAs exposure protocol.

The commercial micro-CT scanner did not provide routine access to the x-ray tube port and collimator assembly, making it impossible to add filtration directly at the x-ray tube port. Filters were fabricated by wrapping copper (0.725 mm) or lead (0.15 mm) foil around an acrylic tube (25-cm outer diameter, 0.64-cm wall thickness); the diameter of the acrylic tube was chosen such that the entire filter assembly could be inserted into the scanner bore, surrounding the object being scanned. Note that in order to avoid gaps

or overlap at the junction, it is important to wrap foil in an integral number of turns; for the copper filtration 9 layers of foil were required and for lead filtration, only one layer was needed. The use of this large cylindrical filter also results in a small variation of filter thickness with fan angle, but this was deemed negligible (1.3% at the maximum fan angle of 9.2°). This arrangement divided the required filtration equally between pre-object and post-object filtration, resulting in 1.45 mm equivalent Cu filtration (and 0.3 mm equivalent Pb filtration) of the x-ray beam at the detector. Note that while this division of filtration into a pre- and post-object filter results in increased x-ray exposure to the specimen, it is equivalent to entirely pre-object filtration, with respect to multiple-energy decomposition.

3.3.3.3 Image acquisition

For all experiments in this study, 1000 projection views were acquired over 360° in 8 seconds; only the middle 360 lines of the 1024 x 1024 detector were read out, resulting in an axial (along the z-axis) and trans-axial field of view of 5.4 cm and 15.4 cm, respectively. Projection images were processed using a cone-beam algorithm[59] to produce a reconstructed 3-D volume with isotropic voxel spacing of 150 μm.[39] Images were acquired for each of the three scan protocols listed in **Table 3-2**. To investigate the effect of noise on material decomposition accuracy, each scan protocol was repeated 10 times. For each scan protocol, averaged 3-D images (3-D isotropic matrices) were generated by averaging n individual image matrices, where n ranged between 1 and 10.

3.3.3.4 Material decomposition

To validate the results obtained in the numerical simulations, material decomposition was performed using the originally reconstructed images and after averaging multiple images together, to a maximum of 10 averaged images. Each pair (or triplet) of averaged images was then decomposed into material-specific images using the algorithms described above. As with the simulated images, the decomposition accuracy was calculated by averaging the signal intensities of five cylindrical ROIs defined in regions known to contain 100% of the representative material in each material-specific image; the ROIs were aligned along the z-axis and contained approximately 400 voxels, 1.35 mm^3 (length = 8 pixels; radius = 4 pixels).

3.3.3.5 Exposure measurement

To characterize the x-ray dose delivered to a specimen or phantom using the dual- or triple-energy protocol, x-ray exposures were measured for each of the scan protocols **(Table 3-3)**. To obtain exposure measurements, the gantry of the scanner was held fixed and a paddle ionization chamber (model 96035, Keithley, Cleveland, OH) placed in the centre of the field of view, perpendicular to, and completely within the x-ray beam. The paddle ionization chamber was connected to a dosimeter (model 35617, Keithley, Cleveland, OH). For each scan protocol (kVp and filtration), the electrical charge (in nC) was recorded by the ion chamber for a 1.1 sec. exposure at 90 mA. Measurement exposure (per mAs) in Roentgens was obtained using the ion-chamber conversion factor of 0.2327 R nC^{-1} and dividing by the exposure mAs. The total absorbed dose (in air), for each protocol, was calculated using a conversion factor of D_{air} = 0.876 cGy R^{-1} for a single scan and a total of six combined scans.[60]

Scan Protocol	Tube Potential (kVp)	Total Added Filtration (mm)	mA	Scan Time (s)	Measured Exposure (mR /mAs)	Absorbed Dose (in air) (cGy) Single Scan	Absorbed Dose (in air) (cGy) Six Scans
1	96	0.3 Pb	160	8	5.1	5.7	34.1
2	140	1.45 Cu	100	8	16.0	11.2	67.3
3	70	0	190	8	9.5	12.7	76.1

Table 3-3 *Absorbed dose (in air) measured for the three scan protocols for one scan and six total scans.*

3.3.4 Application in Microfil-perfused specimen

3.3.4.1 Specimen preparation

Upon successful completion of numerical and phantom studies, the optimized dual- and triple-energy decomposition techniques were applied in a Microfil-perfused rat specimen, which was prepared as part of a separate study. The Sprague-Dawley rat (460 g) was anesthetized using a Ketamine/Xylazine mixture (100mg/Kg and 10mg/Kg body weight, respectively). Heparinized saline (1 ml) was injected via the tail vein to prevent blood coagulation. The abdominal cavity was exposed, the abdominal aorta was canulated and heparinized saline was injected in order to flush all the blood from the vasculature. The Microfil mixture (MV-122, using a mixing ratio of 2:1 - MV diluent to MV compound for decreased viscosity) was then perfused through the vasculature under a pressure of 130 mm Hg. This ratio of diluent to MV compound was used to decrease the viscosity of the fluid being perfused. After the Microfil began to set, the animal and perfusion equipment were left in place for one hour to ensure that the Microfil had completely hardened under a constant pressure of 130 mm Hg. This perfusion technique was modified based on techniques previously employed for vascular casting.[38,61] Following completion of the casting process, the rat was fixed in formalin and stored at

4 °C. All procedures were approved by the Council on Animal Care at the University of Western Ontario.

3.3.4.2 Specimen imaging

Prior to imaging, the rat specimen was warmed to room temperature, vacuum-sealed in a plastic bag and placed on top of an immobilizing bag (VacFix, Par Scientific A/S, Denmark); both the vacuum sealing and immobilization bag prevented sagging and motion of the specimen during scanning. The specimen remained stationary on the scanner bed, while the Pb and Cu filters were interchanged between scans. The specimen was imaged using the optimized dual-energy protocol; at each of the energies (**Table 3-2**), six 3-D images of the specimen were acquired and averaged following reconstruction. To cover the entire head and thoracic region of the rat specimen, a second set of scans was obtained, offset from the first by 4.5 cm, enabling a composite 3-D image to be formed. The reconstructed images were scaled in HU, and ROIs were drawn in regions of the images that contained respective basis materials (cortical bone, Microfil, or soft tissue); the same region was identified in each of the averaged images. Note, that in the case of specimen imaging, the CT values for the representative components can be determined in this manner directly from the reconstructed images, rather than using an additional calibrator phantom. The mean CT number calculated in each of the regions was used as input to the dual-energy material decomposition algorithm. Material-specific images were generated for cortical bone, Microfil, and soft tissue. Images were displayed and analysed using Microview (GE Healthcare, London, ON) and VGStudio Max (Volume Graphics GmbH, Heidelberg, Germany).

3.4 Results

The linear attenuation coefficients of the three basis materials – cortical bone, Microfil, and soft tissue – are plotted as a function of energy in **Figure 3-1**(a). These linear attenuation coefficients were used in the determination of the optimal x-ray spectra, which are plotted in **Figure 3-1**(b). The optimal spectra were determined based on maximizing the contrast difference between cortical bone and Microfil as shown in the plot of the CMCR figure of merit in **Figure 3-2**. With the selected filtration, CMCR was maximized when a maximum x-ray tube potential of 96 kVp was used with the 0.3 mm Pb filter, to block out most of the x-rays above the *K* edge of Pb, and a tube potential of 140 kVp was used with the 1.44-mm Cu filter, which maximizes the x-ray flux at energies above the *K* edge of Pb. Note that for the 3rd energy, the lowest x-ray tube potential was used and no filtration was added. **Table 3-1** summarizes the three scan protocols and lists the mean energies of each.

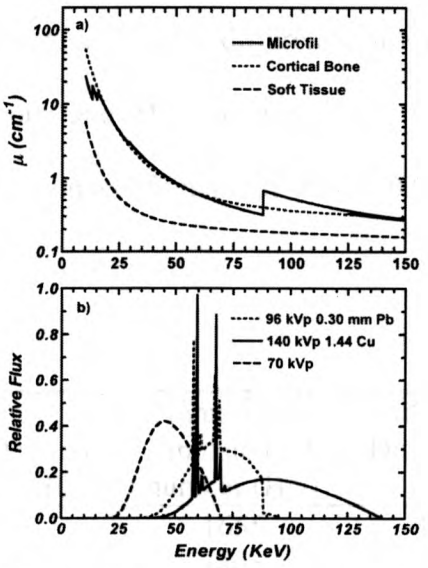

Figure 3-1 *(a) Linear attenuation coefficients of Microfil, cortical bone, and soft tissue. (b) Simulated x-ray spectra of the three scan protocols used in the dual- and triple-energy material decomposition techniques listed in Table 2.2.*

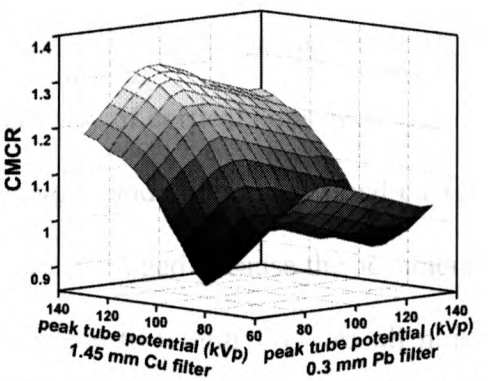

Figure 3-2 *Cortical bone to Microfil contrast ratio (CMCR) evaluated for the dual-energy approach – a range of peak tube potentials was investigated for both the 0.3 mm-Pb-filtered spectrum and the 1.45 mm-Cu-filtered spectrum.*

The simulated CT numbers of the basis materials were verified against the measured CT numbers for the optimal scan protocols listed in **Table 3-2**, and the comparison results are given in **Table 3-3**. The average percent difference between simulated and measured CT number for cortical bone and Microfil was 3.4 ± 1.4% (equivalent to a percent difference in linear attenuation coefficient of 2.1 ± 0.8%), confirming the accuracy of the numerical simulation.

Scan Protocol	kVp / filter	Material	Experimentally derived CT number ± SD (HU)	Numerically simulated CT number (HU)	Absolute Difference (%)
1	96 / Pb	SB3	1600 ± 10	1655	1.9
1	96 / Pb	Microfil	1532 ± 15	1603	4.5
2	140 / Cu	SB3	1300 ± 10	1360	3.4
2	140 / Cu	Microfil	1565 ± 10	1644	4.9
3	70	SB3	3024 ± 14	2969	4.5
3	70	Microfil	3433 ± 11	3387	1.4

Table 3-4 *Comparison of the numerically simulated CT numbers for SB3 (cortical bone) and Microfil to experimentally observed values.*

Based on the numerical simulations, the decomposition accuracy for the soft-tissue images was 99.9 ± 0.1% for all levels of added Gaussian noise (up to 30 HU). **Figure 3-3** is a plot of the average decomposition accuracy of cortical bone and Microfil as a function of noise, for both the triple-energy and optimized dual-energy decomposition; the accuracy for Microfil and bone were averaged because the accuracies achieved for both material-specific images were the same to within 1%. At all noise levels simulated, the decomposition accuracy was greater than 95 %; the error bars in **Figure 3-3** provide an indication of the variability in the achieved accuracy. Note that for the numerical simulation, no significant improvement in accuracy was observed when the third energy was added.

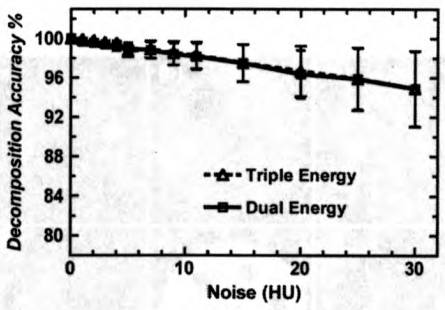

Figure 3-3 *Numerical simulation, showing decomposition accuracy for the dual- and triple-energy algorithms, implemented at increasing Gaussian noise levels.*

The results of the experimental verification of the decomposition algorithms, using the acrylic-bone-Microfil phantom are summarized in **Figure 3-4**, where axial images of the phantom, acquired with the three scan protocols, are shown (**Figure 3-4** (a), (b), and (c)) along with material specific decompositions for cortical bone (d,g), acrylic (e,h), and Microfil (f,i) obtained following dual- and triple-energy decomposition, respectively. For the images in this figure, all 10 acquired images were averaged for each scan protocol; the mean noise in the averaged images used in the dual-energy decomposition was ±11.3 HU. The effect of decreased image noise on the experimentally achieved decomposition accuracy is shown in **Figure 3-5**(a) for dual and triple-energy decomposition; **Figure 3-5**(b) is a plot of the decomposition accuracy of the two techniques expressed as a function of the number of scans averaged to achieve the levels of noise listed in **Figure 3-5**(a). As expected, the accuracy of decomposition improves with increasing number of images averaged. For the dual-energy decomposition, accuracy improves by only 1% when the number of scans averaged increases from 6 to 10. Although the accuracy of the triple energy decomposition is consistently higher than that of dual-energy decomposition for the same number for scans averaged, the increase is not statistically different between a dual-energy decomposition acquired with 6 scans averaged and triple-energy decomposition results acquired with 6 or fewer averages (two-tailed t-test, $p = 0.65$).

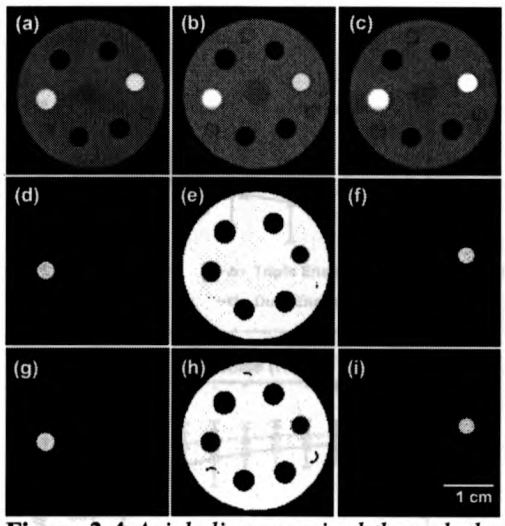

Figure 3-4 *Axial slices acquired through the phantom with the three different scan protocols: (a) 96 kVp 0.3 mm Pb, (b) 140 kVp 1.45 mm Cu, (c) 70 kVp no added filtration; Results of the dual-energy decomposition: (d) Microfil, (e) soft tissue, (f) SB3 Results of the triple energy decomposition: (g) Microfil, (h) soft tissue, (i) SB3.*

The results of the dual-energy decomposition of bone and Microfil of a rat specimen are shown in **Figure 3-6** and **Figure 3-7**. **Figure 3-6** shows maximum intensity projections (MIPs) through the volume CT images of the rat specimen obtained using scan protocol 1 (a) and scan protocol 2 (b), which clearly demonstrate the inability to separate Microfil from cortical bone based on CT number alone. **Figure 3-6**(c) is a MIP through the Microfil-only image decomposed from the images acquired in (a) and (b), while **Figure 3-6**(d) is a MIP through the bone-only image. The separation of cortical bone and Microfil in a single-energy image is particularly difficult in regions where vessels traverse through bone, as is illustrated in **Figure 3-7**(a); the excellent separation achieved by dual-energy decomposition is seen in **Figure 3-7**(b), where the vessel image (Microfil) is colour-coded and overlaid on the cortical-bone image. The intricate network of vessels is very clearly observed in **Figure 3-7**(c), which is a volume rendering of the bone and Microfil images.

3.5 Discussion

We have developed and implemented post-reconstruction dual- and triple-energy material decomposition techniques using a cone-beam micro-CT scanner. Because the decomposition techniques were designed to segment bone from contrast-enhanced vessels (which contain a Pb-based opacifier), the x-ray spectra of the dual-energy approach were designed to have mean energies close to the *K* edge of Pb, with one of the spectra having proportionately higher number of x rays above the *K* edge of Pb. To filter out x-rays above the *K* edge of Pb, a Pb filter was inserted in the x-ray beam, while a Cu filter was used to preferentially filter out lower energy x rays, thereby increasing the mean energy near the *K* edge of Pb. The addition of a scan acquired at a third (low) energy was investigated as well. Both decomposition techniques yielded high accuracy when decomposing images acquired of a phantom and excised specimens into material-specific images of cortical bone, vessels (Microfil), and soft tissue.

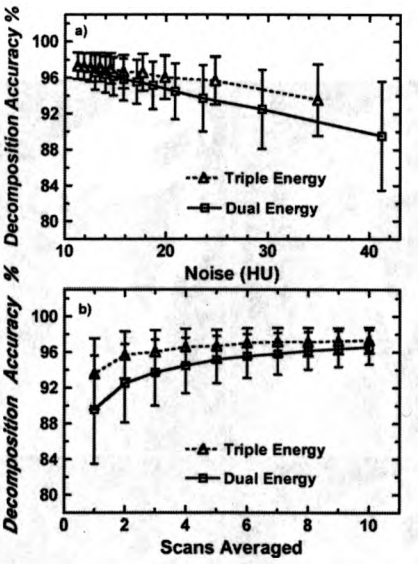

Figure 3-5 *Experimental results, determined from images of the phantom, for the triple-energy and optimized dual-energy decomposition of cortical bone and Microfil. Decomposition accuracy is plotted as a function of average noise (a) and as a function of the number of images averaged, which is linearly proportional to total scan time and dose. The error bars represent the standard error of the mean.*

The material decomposition techniques presented can be implemented on any CT scanner capable of delivering sufficient x-ray fluence at energies greater than 90 kVp, without requiring access to the raw projection data or modifications to the internal

scanner hardware. The method employed for filtering of the x-ray beam, which was achieved simply by surrounding the specimen by a cylinder of uniform thickness of filter material, can be easily adapted on any scanner, even if access to the x-ray tube filter port is not available. Although this approach cannot be used in clinical applications, the added dose due to post-object filtration in the case of specimen imaging was not of concern. A secondary consideration, when implementing this type of filter, would be to ensure that the distances between the filter and the detector and the filter and object are maximized, to minimize the effect of scatter.

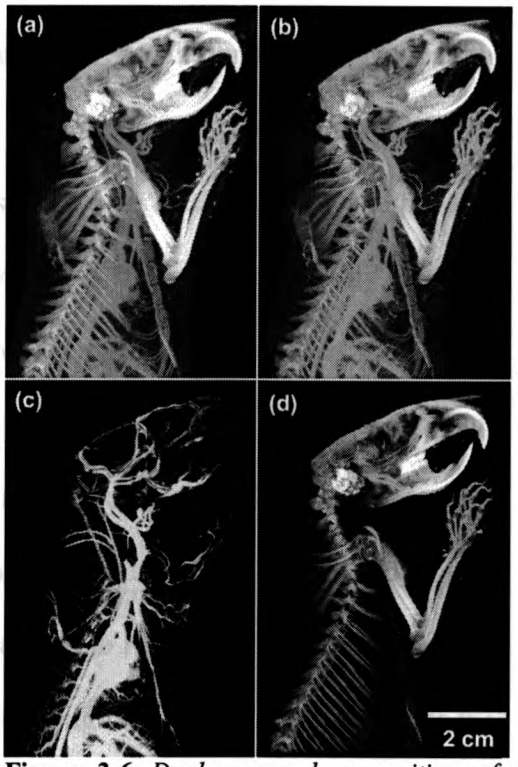

Figure 3-6 *Dual-energy decomposition of cortical bone and Microfil-filled vessels in a rat specimen. Maximum intensity projections through the volume acquired using scan protocol 1 (a) and scan protocol 2 (b) demonstrate the difficulty in separating Microfil and bone, based on CT number alone. MIPs through the Microfil-only decomposed image (c) and the cortical-bone image (d) show the clear separation of vessels and bone. Note the vessels that line the spine in (c) that have been clearly separated from the bone. These vessels are seen in cross-section in Figure 3.7 (b).*

The x-ray spectra used in the dual-energy approach were selected to maximize the contrast difference between Microfil and cortical bone in the two image sets, using the CMCR figure of merit (Eq. 5). For energies above the *K* edge of Pb, the CMCR (**Figure 3-2**) increased monotonically with increasing kVp of the Cu-filtered spectrum, indicating that the highest kVp available on a scanner should be used with the Cu filter. Although CMCR peaked at 96 kVp with the Pb filter, the figure of merit is not as sensitive to the kVp of the Pb-filtered spectrum.

Both dual- and triple-energy approaches yielded cortical bone and Microfil decomposition accuracies greater than 90% even when the noise in the acquired images was as high as ±30 HU. Improvement of decomposition accuracy was achieved by averaging multiple images to reduce noise. Numerical simulations predicted that the improvement of decomposition accuracy for the triple-energy algorithm would be the same as that for the dual-energy algorithm, at noise levels up to ±30 HU. The equivalent phantom experiments demonstrated a consistently higher, but not significantly different, accuracy when images acquired with the third (low) energy were introduced. This small discrepancy between the numerical (**Figure 3-3**) and experimental (**Figure 3-5**) results can be attributed to the fact that the numerical simulations assumed uniform material composition throughout the sample and did not include the effects of beam hardening or scatter. The same effects also contribute to the inability to reach 100% decomposition in the experimental setting, even when image noise is negligible. It is important to note that the implemented decomposition approach is not highly sensitive to inconsistency in the composition of the true materials, because the technique is "self calibrating", i.e. the CT numbers of the basis materials are identified within the acquired images by an operator.

Based on the phantom results, we chose to perform further material decompositions using the dual-energy approach, with 6 images averaged per scan protocol. The phantom results indicated that decomposition accuracy greater than 95% can be achieved, when the noise in the averaged CT images was greater than 17 HU and an improvement of only a few percent was achievable if image noise was reduced further through the averaging of extra images. Although an equivalent accuracy can be achieved using the triple-energy approach when averaging only two images per scan protocol (for a total of 6 images), we chose the dual-energy approach (with 6 images at each of the two energies) because of the simplicity of the algorithm and reducing the chance of moving the specimen between scans while replacing filters. Similarly, we chose not to attempt to improve the decomposition accuracy of the rat specimen by averaging more than six images, given that the improvement in accuracy was small. In future applications of material decompositions of this type, if switching of the filter configuration could be achieved without increasing the risk of moving the specimen, the acquisition of triple energy scans will result in slight improvements in decomposition accuracy or a reduction in dose (of as much as 30%) for the same

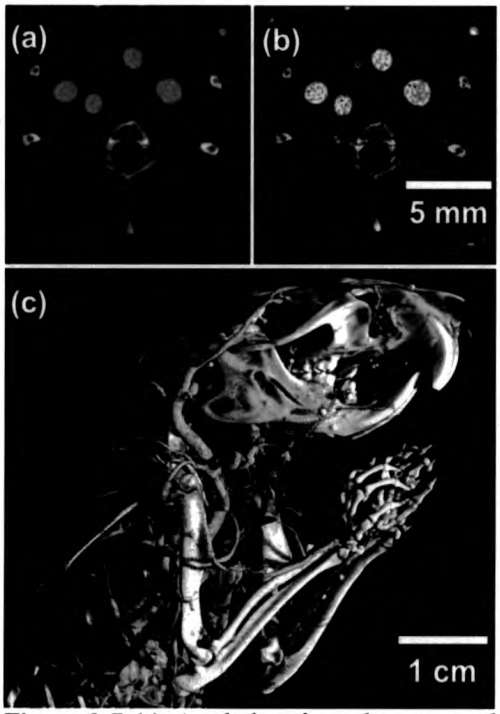

Figure 3-7 (a) *Axial slice from the averaged volume acquired at 96 kVp (0.3 mm Pb filtration) demonstrating the difficulty in distinguishing bone from Microfil, (b) the same axial slice overlaid with the vessel-only image, clearly showing the vessels entering the vertebral spaces, (c) volume rendered image of the Microfil-only and bone-only images demonstrating the excellent separation and complex geometry of the vascular network.*

accuracy. More significant improvements in the accuracy of vessel (Microfil) segmentation from adjacent bone could be achieved by combining the dual-energy approach with more advanced rule-based segmentation algorithms, such as region-growing, connectivity, or adaptive thresholding.[62]

In this study we implemented the dual- and triple-energy techniques specifically for the separation of two materials (cortical bone and Microfil) commonly encountered when imaging post-mortem specimens. In the implementation used to generate the material-specific images in **Figure 3-6** and **Figure 3-7** the cumulative dose (from all 12 scans) to the specimen was 1.0 Gy. Although this dose may be high for longitudinal experiments in live animals, it is appropriate for imaging specimens. To be applicable for imaging live animals, the technique must be adapted for use with injectable contrast materials (commonly iodine based); in this case the filters must be designed to produce spectra that straddle the *K* edge of iodine. Dose reduction to the animal could be achieved by implementing a filter-exchange mechanism at the x-ray tube port, thereby removing the post-object filtration. Furthermore, if a slightly lower (but still greater than 90%) decomposition accuracy is acceptable for a particular application, the number of images averaged could be reduced, resulting in dose as low as 0.16 Gy (for 2 averaged images using the dual-energy approach, and resulting in an accuracy of 92%).

Our protocol for post-mortem imaging of small-animals can be compared with the recently reported implementation of dual-source, dual-energy CT for bone-iodine material differentiation in human subjects.[16,63] In this clinical application, optimization of

the low- and high-energy x-ray spectra (80 and 140 kVp, respectively) resulted in a lower mean energy for the low-energy acquisition than in our study; this is to be expected, due to the fact that the *K* edge of iodine (33 keV) is considerably lower that that of lead (88 keV). The exposure for the clinical protocol (8 mGy) was also significantly lower than that reported in our study (1000 mGy); this observation is consistent with the significant difference in voxel volume. In vivo investigations in humans are typically carried out with voxel volumes of approximately 1 mm^3, while the nominal voxel volume in our study was a factor of 220 times smaller (0.0034 mm^3). Previous studies have shown that the dose in computed tomography increases non-linearly with decreasing voxel volume, if image noise is maintained constant.[64-66] Note that these exposure measurements were made with the spectra optimized for cortical bone/Microfil separation and the values will be different when optimizing for cortical bone/iodine separation.

The decomposition of the specimen images into a Microfil-only and bone-only image (**Figure 3-6** and **Figure 3-7**) was highly effective and enables complete separation of the vessels from the bone (**Figure 3-7** (b,c)). Because Microfil concentration may vary, due to inconsistencies of preparation or slight clumping of the pigment, it is important to identify regions of interest that best describe the mean attenuation of Microfil when selecting the attenuation coefficient for "pure" Microfil to use as the input to the dual-energy decomposition. If regional variations exist, the region of the respective basis material must be selected within the anatomical region of interest. The bone-only image (**Figure 3-6** (d)) shows variations in the percentage of cortical bone present within different anatomical features. This was expected, since the bones do not

consist of 100% cortical bone; trabecular bone regions are correctly classified as having a lower bone fraction and highly mineralized regions, such as the teeth and inner ear, appear as bright regions in the image. These highly mineralized tissues in fact represent a fourth material in the decomposition, but are nonetheless accurately defined as being "bone-like" rather than "Microfil-like" because of the ratio of the attenuation coefficients of these materials at the two energies is most similar to that of cortical bone.

The technique described in this manuscript represents the first post-reconstruction application of a material-specific decomposition that directly takes advantage of the *K* edge characteristics of a contrast material injected into an animal specimen. Using this approach, accurate segmentation of the 3-D image into bone and vessel components was achieved entirely automatically, facilitating quantitation of vessel density and architecture near bone. The research applications of such a technique are numerous, especially in the study of osteoarthritis and the involvement of the vasculature in disease progression and regression.[6,67] We have demonstrated that both the dual-energy and triple-energy techniques result in highly accurate decompositions of two materials that would otherwise be indistinguishable by CT-number based segmentation.

3.6 References

1 G. L. Kindlmann, D. M. Weinstein, G. M. Jones, C. R. Johnson, M. R. Capecchi, and C. Keller, "Practical vessel imaging by computed tomography in live transgenic mouse models for human tumors", Mol Imaging **4**, 417-424 (2005).

2 E. L. Ritman, "Molecular imaging in small animals--roles for micro-CT", J Cell Biochem Suppl **39**, 116-124 (2002).

3 D. W. Holdsworth, "Micro-CT in small animal and specimen imaging", Trends in Biotechnology **20**, S34-S39 (2002).

4 M. J. Paulus, S. S. Gleason, S. J. Kennel, P. R. Hunsicker, and D. K. Johnson, "High resolution X-ray computed tomography: an emerging tool for small animal cancer research", Neoplasia **2**, 62-70 (2000).

5 E. B. Walters, K. Panda, J. A. Bankson, E. Brown, and D. D. Cody, "Improved method of in vivo respiratory-gated micro-CT imaging", Phys Med Biol **49**, 4163-4172 (2004).

6 D. D. McErlain, C. T. Appleton, R. B. Litchfield, V. Pitelka, J. L. Henry, S. M. Bernier, F. Beier, and D. W. Holdsworth, "Study of subchondral bone adaptations in a rodent surgical model of OA using in vivo micro-computed tomography", Osteoarthritis Cartilage **16**, 458-469 (2008).

7 C. T. Appleton, D. D. McErlain, V. Pitelka, N. Schwartz, S. M. Bernier, J. L. Henry, D. W. Holdsworth, and F. Beier, "Forced mobilization accelerates pathogenesis: characterization of a preclinical surgical model of osteoarthritis", Arthritis Res Ther **9**, R13 (2007).

8 M. D. Bentley, M. C. Ortiz, E. L. Ritman, and J. C. Romero, "The use of microcomputed tomography to study microvasculature in small rodents", Am J Physiol Regul Integr Comp Physiol **282**, R1267-1279 (2002).

9 L. A. Feldkamp, S. A. Goldstein, A. M. Parfitt, G. Jesion, and M. Kleerekoper, "The direct examination of three-dimensional bone architecture in vitro by computed tomography", J Bone Miner Res **4**, 3-11 (1989).

10 A. Barbier, C. Martel, M. C. de Vernejoul, F. Tirode, M. Nys, G. Mocaer, C. Morieux, H. Murakami, and F. Lacheretz, "The visualization and evaluation of bone architecture in the rat using three-dimensional X-ray microcomputed tomography", J Bone Miner Metab **17**, 37-44 (1999).

11 Y. Jiang, J. Zhao, D. L. White, and H. K. Genant, "Micro CT and Micro MR imaging of 3D architecture of animal skeleton", J Musculoskelet Neuronal Interact **1**, 45-51 (2000).

12 A. C. Langheinrich, J. Wienhard, S. Vormann, B. Hau, R. M. Bohle, and M. Zygmunt, "Analysis of the fetal placental vascular tree by X-ray micro-computed tomography", Placenta **25**, 95-100 (2004).

13 W. W. Lam, D. W. Holdsworth, L. Y. Du, M. Drangova, D. G. McCormack, and G. E. Santyr, "Micro-CT imaging of rat lung ventilation using continuous image

acquisition during xenon gas contrast enhancement", J Appl Physiol **103**, 1848-1856 (2007).

14 N. L. Ford, K. C. Graham, A. C. Groom, I. C. Macdonald, A. F. Chambers, and D. W. Holdsworth, "Time-course characterization of the computed tomography contrast enhancement of an iodinated blood-pool contrast agent in mice using a volumetric flat-panel equipped computed tomography scanner", Invest Radiol **41**, 384-390 (2006).

15 Philip Engler and William D. Friedman, "Review of dual-energy computed tomography techniques", Materials Evaluation **48**, 623-629 (1990).

16 A. Graser, T. R. Johnson, M. Bader, M. Staehler, N. Haseke, K. Nikolaou, M. F. Reiser, C. G. Stief, and C. R. Becker, "Dual energy CT characterization of urinary calculi: initial in vitro and clinical experience", Invest Radiol **43**, 112-119 (2008).

17 W. Marshall, E. Hall, A. Doost-Hoseini, R. Alvarez, A. Macovski, and D. Cassel, "An implementation of dual energy CT scanning", J Comput Assist Tomogr **8**, 745-749 (1984).

18 W. A. Kalender, W. H. Perman, J. R. Vetter, and E. Klotz, "Evaluation of a prototype dual-energy computed tomographic apparatus. I. Phantom studies", Med Phys **13**, 334-339 (1986).

19 R. E. Alvarez and A. Macovski, "Energy-selective reconstructions in X-ray computerized tomography", Phys Med Biol **21**, 733-744 (1976).

20 M. R. Millner, W. D. McDavid, R. G. Waggener, M. J. Dennis, W. H. Payne, and V. J. Sank, "Extraction of information from CT scans at different energies", Med Phys **6**, 70-71 (1979).

21 A. J. Coleman and M. Sinclair, "A beam-hardening correction using dual-energy computed tomography", Phys Med Biol **30**, 1251-1256 (1985).

22 L. A. Lehmann, R. E. Alvarez, A. Macovski, W. R. Brody, N. J. Pelc, S. J. Riederer, and A. L. Hall, "Generalized image combinations in dual KVP digital radiography", Med Phys **8**, 659-667 (1981).

23 P. Stenner, T. Berkus, and M. Kachelriess, "Empirical dual energy calibration (EDEC) for cone-beam computed tomography", Med Phys **34**, 3630-3641 (2007).

24 S. M. Midgley, "Materials analysis using x-ray linear attenuation coefficient measurements at four photon energies", Phys Med Biol **50**, 4139-4157 (2005).

25 R. Lawaczeck, F. Diekmann, S. Diekmann, B. Hamm, U. Bick, W. R. Press, H. Schirmer, K. Schon, and H. J. Weinmann, "New contrast media designed for x-ray energy subtraction imaging in digital mammography", Invest Radiol **38**, 602-608 (2003).

26 S. J. Riederer, R. A. Kruger, C. A. Mistretta, D. L. Ergun, and C. G. Shaw, "Three-beam K-edge imaging of iodine using differences between fluoroscopic video images: experimental results", Med Phys **8**, 480-487 (1981).

27 A. Sarnelli, H. Elleaume, A. Taibi, M. Gambaccini, and A. Bravin, "K-edge digital subtraction imaging with dichromatic x-ray sources: SNR and dose studies", Phys Med Biol **51**, 4311-4328 (2006).

28 R. A. Kruger, C. A. Mistretta, A. B. Crummy, J. F. Sackett, M. M. Goodsitt, S. J. Riederer, T. L. Houk, C. G. Shaw, and D. Fleming, "Digital K-edge subtraction radiography", Radiology **125**, 243-245 (1977).

29 S. J. Riederer and C. A. Mistretta, "Selective iodine imaging using K-edge energies in computerized x-ray tomography", Med Phys **4**, 474-481 (1977).

30 E. Roessl and R. Proksa, "K-edge imaging in x-ray computed tomography using multi-bin photon counting detectors", Phys Med Biol **52**, 4679-4696 (2007).

31 P. Sukovic and N. H. Clinthorne, "Penalized weighted least-squares image reconstruction for dual energy X-ray transmission tomography", IEEE Trans Med Imaging **19**, 1075-1081 (2000).

32 P. Dawson, "X-ray contrast-enhancing agents", Eur J Radiol **23**, 172-177 (1996).

33 C. T. Badea, L. W. Hedlund, M. De Lin, J. F. Boslego Mackel, and G. A. Johnson, "Tumor imaging in small animals with a combined micro-CT/micro-DSA system using iodinated conventional and blood pool contrast agents", Contrast Media Mol Imaging **1**, 153-164 (2006).

34 A. N. Cheema, T. Hong, N. Nili, A. Segev, J. G. Moffat, K. E. Lipson, A. R. Howlett, D. W. Holdsworth, M. J. Cole, B. Qiang, F. Kolodgie, R. Virmani, D. J. Stewart, and B. H. Strauss, "Adventitial microvessel formation after coronary stenting and the effects of SU11218, a tyrosine kinase inhibitor", J Am Coll Cardiol **47**, 1067-1075 (2006).

35 M. Marxen, M. M. Thornton, C. B. Chiarot, G. Klement, J. Koprivnikar, J. G. Sled, and R. M. Henkelman, "MicroCT scanner performance and considerations for vascular specimen imaging", Med Phys **31**, 305-313 (2004).

36 P. E. Beighley, P. J. Thomas, S. M. Jorgensen, and E. L. Ritman, "3D architecture of myocardial microcirculation in intact rat heart: a study with micro-CT", Adv Exp Med Biol **430**, 165-175 (1997).

37 A. Garcia-Sanz, A. Rodriguez-Barbero, M. D. Bentley, E. L. Ritman, and J. C. Romero, "Three-dimensional microcomputed tomography of renal vasculature in rats", Hypertension **31**, 440-444 (1998).

38 J. W. Xuan, M. Bygrave, H. Jiang, F. Valiyeva, J. Dunmore-Buyze, D. W. Holdsworth, J. I. Izawa, G. Bauman, M. Moussa, S. F. Winter, N. M. Greenberg, J. L. Chin, M. Drangova, A. Fenster, and J. C. Lacefield, "Functional neoangiogenesis imaging of genetically engineered mouse prostate cancer using three-dimensional power Doppler ultrasound", Cancer Res **67**, 2830-2839 (2007).

39 L. Y. Du, J. Umoh, H. N. Nikolov, S. I. Pollmann, T. Y. Lee, and D. W. Holdsworth, "A quality assurance phantom for the performance evaluation of volumetric micro-CT systems", Phys Med Biol **52**, 7087-7108 (2007).

40 W. Ross, D. D. Cody, and J. D. Hazle, "Design and performance characteristics of a digital flat-panel computed tomography system", Med Phys **33**, 1888-1901 (2006).

41 S. Greschus, F. Kiessling, M. P. Lichy, J. Moll, M. M. Mueller, R. Savai, F. Rose, C. Ruppert, A. Gunther, M. Luecke, N. E. Fusenig, W. Semmler, and H. Traupe, "Potential applications of flat-panel volumetric CT in morphologic and functional small animal imaging", Neoplasia **7**, 730-740 (2005).

42 F. Kiessling, S. Greschus, M. P. Lichy, M. Bock, C. Fink, S. Vosseler, J. Moll, M. M. Mueller, N. E. Fusenig, H. Traupe, and W. Semmler, "Volumetric computed tomography (VCT): a new technology for noninvasive, high-resolution monitoring of tumor angiogenesis", Nat Med **10**, 1133-1138 (2004).

[43] M. Drangova, N. L. Ford, S. A. Detombe, A. R. Wheatley, and D. W. Holdsworth, "Fast Retrospectively Gated Quantitative Four-Dimensional (4D) Cardiac Micro Computed Tomography Imaging of Free-Breathing Mice", Invest Radiol **42**, 85-94 (2007).

[44] K. C. Graham, N. L. Ford, L. T. MacKenzie, C. O. Postenka, A. C. Groom, I. C. MacDonald, D. W. Holdsworth, M. Drangova, and A. F. Chambers, "Noninvasive quantification of tumor volume in preclinical liver metastasis models using contrast-enhanced x-ray computed tomography", Invest Radiol **43**, 92-99 (2008).

[45] N. L. Ford, A. R. Wheatley, D. W. Holdsworth, and M. Drangova, "Optimization of a retrospective technique for respiratory-gated high speed micro-CT of free-breathing rodents", Phys Med Biol **52**, 5749-5769 (2007).

[46] J. Missbach-Guentner, C. Dullin, M. Zientkowska, M. Domeyer-Missbach, S. Kimmina, S. Obenauer, F. Kauer, W. Stuhmer, E. Grabbe, W. F. Vogel, and F. Alves, "Flat-panel detector-based volume computed tomography: a novel 3D imaging technique to monitor osteolytic bone lesions in a mouse tumor metastasis model", Neoplasia **9**, 755-765 (2007).

[47] S. Obenauer, C. Dullin, and M. Heuser, "Flat panel detector-based volumetric computed tomography (fpVCT): performance evaluation of volumetric methods by using different phantoms in comparison to 64-multislice computed tomography", Invest Radiol **42**, 291-296 (2007).

[48] H. J. Vinegar and S. L. Wellington, "Tomographic imaging of three-phase flow experiments", Rev. Sci. Instrum. **58**, 96-107 (1987).

[49] Xiaoheng Liu Yaping Zhou Xujie Yang Lude Lu Xin Wang Daoyong Chen, "Grid search as applied to the determination of Mark-Houwink parameters", Journal of Applied Polymer Science **76**, 481-487 (2000).

[50] D. M. Tucker, G. T. Barnes, and D. P. Chakraborty, "Semiempirical model for generating tungsten target x-ray spectra", Med Phys **18**, 211-218 (1991).

[51] D. M. Tucker, G. T. Barnes, and X. Z. Wu, "Molybdenum target x-ray spectra: a semiempirical model", Med Phys **18**, 402-407 (1991).

[52] J. A. Rowlands and K. W. Taylor, "Absorption and noise in cesium iodide x-ray image intensifiers", Med Phys **10**, 786-795 (1983).

[53] P. R. Granfors and R. Aufrichtig, "Performance of a 41X41-cm2 amorphous silicon flat panel x-ray detector for radiographic imaging applications", Med Phys **27**, 1324-1331 (2000).

[54] W. Zhao, G. Ristic, and J. A. Rowlands, "X-ray imaging performance of structured cesium iodide scintillators", Med Phys **31**, 2594-2605 (2004).

[55] ICRU Report 44, Tissue Substitutes in Radiation Dosimetry and Measurement, 1989.

[56] M.J. Berger, J.H. Hubbell, S.M. Seltzer, J. Chang, Coursey J.S., R. Sukumar, and Zucker D.S., "National Institutes of Standards and Technology Photon Cross Sections Database " (1998).

[57] G.E.P. Box and E. Muller, "A Note on the Generation of Random Normal Deviates", Annals of Mathematical Statistics **29**, 610-611 (1958).

[58] D. R. White, "Tissue substitutes in experimental radiation physics", Med Phys **5**, 467-479 (1978).

[59] L. A. Feldkamp, L. C. Davis, and J.W. Kress, "Practical cone-beam algorithm", Opt. Sci. Am. A. **1**, 612-619 (1984).

[60] J. F. Valley and P. Lerch, "Letter: Dose conversion factors at the calibration beam energy", Phys Med Biol **18**, 744-746 (1973).

[61] Y. Q. Zhou, L. Davidson, R. M. Henkelman, B. J. Nieman, F. S. Foster, L. X. Yu, and X. J. Chen, "Ultrasound-guided left-ventricular catheterization: a novel method of whole mouse perfusion for microimaging", Lab Invest **84**, 385-389 (2004).

[62] J. H. Waarsing, J. S. Day, and H. Weinans, "An improved segmentation method for in vivo microCT imaging", J Bone Miner Res **19**, 1640-1650 (2004).

[63] T. R. Johnson, B. Krauss, M. Sedlmair, M. Grasruck, H. Bruder, D. Morhard, C. Fink, S. Weckbach, M. Lenhard, B. Schmidt, T. Flohr, M. F. Reiser, and C. R. Becker, "Material differentiation by dual energy CT: initial experience", Eur Radiol **17**, 1510-1517 (2007).

[64] N. L. Ford, M. M. Thornton, and D. W. Holdsworth, "Fundamental image quality limits for microcomputed tomography in small animals", Med Phys **30**, 2869-2877 (2003).

[65] K. Faulkner and B. M. Moores, "Noise and contrast detection in computed tomography images", Phys Med Biol **29**, 329-339 (1984).

[66] R. A. Brooks and G. Di Chiro, "Statistical limitations in x-ray reconstructive tomography", Med Phys **3**, 237-240 (1976).

[67] L. de Saint-Georges and S. C. Miller, "The microcirculation of bone and marrow in the diaphysis of the rat hemopoietic long bones", Anat Rec **233**, 169-177 (1992).

Chapter 4: Summary and Related Future Directions

4.1 Summary

In summary, I have demonstrated that micro-CT is a powerful tool for qualitative imaging, but also for quantitative measurements of tissues and bone mineral content. Furthermore, by micro-CT imaging of an entire rat specimen, I have demonstrated the ability to accurately calculate the total weight of rats by their CT image alone. In addition, I have shown that a current micro-CT imaging system can report these measurements to a high degree of precision.

Identifying tissues by their CT image intensity alone (such as adipose tissue, lean tissue, and bone, as demonstrated in chapter 2) highlights the capability of traditional (*single-energy*) computed tomography to perform material segmentation by greyscale thresholds. The ability to precisely quantify tissues in micro-CT images of rodents should make this technique highly desirable in drug investigations that monitor physiological changes in murine phenotypes. An additional benefit to drug investigations is that current micro-CT imaging systems possess the speed and processing power to image large numbers of specimens while maintaining a reasonable cost, in our case approximately $100 per rat.

However, in certain circumstances, a need to image a specimen at two or more X ray energies may be required for improved material segmentation; for example, as we

have successfully demonstrated in chapter 3, between contrast-enhanced vessel and bone, using dual-and triple-energy CT acquisition data. The novelty in our approach – using a cylindrical filter insert in combination with different tube potentials to achieve sufficiently different X-ray spectra – should not be understated, since it can be applied to any existing small animal micro-CT scanner without any modifications to the hardware or access to the pre-reconstruction data. Moreover, we have shown that a dual-source CT device is not required to perform dual energy experiments in post mortem specimens.

Furthermore, by extending a dual-energy decomposition algorithm into a triple-energy algorithm for material decomposition as shown in chapter 3, we have found it somewhat advantageous to acquire three energies over two energies, in cases where dose considerations may apply. In demonstrating an advantage in acquiring three energies over two energies in our material decomposition scheme, it points out that many previous decomposition algorithm schemes, which only acquire two x-ray measurements at different energies, may not be taking full advantage of energy-dependent CT data information.

While this paper has primarily focused on the technical aspects of material classification schemes – using traditional and novel dual- and triple-energy CT acquisitions – the resulting material-specific data provides a wealth of information to be studied. For example, the decomposed vessel-only image from chapter 3 can now be used to study vessel volume fraction, or vascular anatomy such as vessel tortuousity.[1] Vascular anatomy analysis near bone would also be quite valuable for disease investigations such

as preclinical small-animal osteoarthritis models; in these studies, researchers are interested in the subtle changes in vascularity in bones near the joint.[2]

4.2 Related Future Directions

4.2.1 Preclinical Uses

4.2.1.1 Fabricated Contrast Mediums

While there have been many early studies investigating appropriate contrast agents for use in clinical radiographic applications, the medical industry has demonstrated a reluctance, albeit justified – given the potential toxicity to patients – to expand past the current chemical variety available. However, a wide variety of contrast agents, used specifically in sacrificed animal specimens, could be commercially developed and designed to take advantage of sharp *K*-edges from high-Z chemicals. Potential chemicals could include tin, or more exotic materials like erbium, where the *K*-edge at 57 KeV falls in the middle of the mean energy of typical x-ray spectra (80 kVp).

4.2.2 Clinical Developments

As I have demonstrated earlier, dual-energy CT measurements are possible, using sacrificed animal specimens from a single-energy micro-CT x-ray source; however, live animal specimens present a significant hurdle for dual-energy image registration. The technical obstacle is acquiring dual-energy measurements that are not susceptible to object motion, which has been investigated earlier with a few main design solutions proposed; these technologies are referred to as: rapid kVp switching, dual-energy detector, or dual-source computed tomography (DSCT).

Surprisingly, as early as the 1980s, a rapid kVp switching x-ray source had been implemented and commercially developed in the Siemens Somatom DR3 series.[3,4] In this configuration, two different energy x-ray transmission measurements are obtained in each projection by rapidly switching the tube potential. However, this device was found to be too narrow in its approach, obtaining only single-slice images in long acquisition times, unlike the subsequent capabilities of slip-ring technology.

Dual-Energy detectors using a layered or "sandwich" strategy for x-ray imaging were also developed early in the development of CT. In general, this type of detector works primarily by collecting an initial "soft" or low-energy spectrum followed by a "harder" or high-energy spectrum. This type of configuration is ideal, since the dual-energy images would be acquired simultaneously, eliminating any registration artefact between two images. At present, studies have shown that due to the difficulty in separating spectral frequencies, these detectors have a lower signal-to-noise ratio over imaging with dual spectra.[5,6]

The first commercial dual-source CT imaging system was only recently developed (2005) and realized in Siemens' Somatoma Definition (Siemens AG, Medical Solutions Computed Tomography, Forchheim, Germany).[7] As the name would suggest, a dual-source CT system is comprised of two x-ray sources and two detectors mounted perpendicular to each other on a gantry. The commercial production of this dual-source system has garnered renewed interest in dual-energy computed tomography, and its extended applications, particularly in *in vivo* imaging of the beating heart.[8]

4.2.2.1 Clinical Dual-Energy Applications

At present, Siemens is touting a number of clinical benefits for patients when scanned using the first dual-source CT system and dual-energy techniques. One benefit, which is analogous to my study, is an automatic bone subtraction from contrast-enhanced vessels in human patients using an iodine-based contrast agent, as shown in **Figure 4-1**.

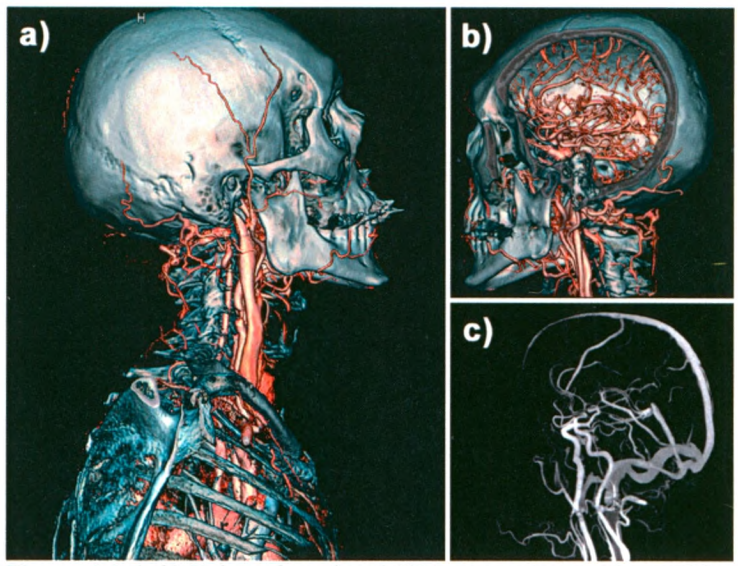

Figure 4-1 *(a,b) Volumed rendered CT images, showing bone-iodine separation using Siemens' Somatom Definition dual-source CT device. (c) Volume rendered iodine only image. X-ray tubes operate at 80 and 120 kVp. Permisson obtained by David Menary, Internal Communications, Siemens Canada Limited.*

Another promising clinical application for dual-energy CT using this dual-source CT system is *in vivo* kidney stone characterization. In this application, the dual-source CT system will identify kidney stones as either calcium or uric acid-based. Once a kidney stone has been characterized *in vivo*, appropriate diagnosis and treatment can be assigned; ultimately, improving the quality of life for patients.

4.2.2.2 Mummy Investigation

Beyond the clinical relevance of dual-energy CT, are a host of other applications, particularly in geology, materials science and archeology. Since CT is a non-destructive

technique for 3-D imaging of anatomical structures within specimens and patients, it is often used to interrogate mummified remains.

A recent research project at the University of Western Ontario involves an adult female Egyptian mummy (XX1st dynasty) on loan from the Royal Ontario Museum (ROM 910.5.3) for bioarchaeological analysis. The analysis will include both traditional and new radiological techniques (specifically dual-and triple-energy computed tomography) in hopes to gain further insight into the life and history of the mummy.

While a full report has yet to be completed, three head scans of the adult female mummy were obtained using the GE Lightspeed clinical 64-slice CT scanner (GE Healthcare, Waukesha, Wisconsin, USA) at University Hospital, in London, Ontario. The single-second scans used tube potentials of 80, 100, and 140 kVp and a tube current of 675 mA for each.

Using the techniques I described in chapter 3, a triple-energy material decomposition was performed on the three reconstructed images for basis materials: teeth (dentin and enamel); skull (mandible); and all exterior materials (soft tissue, wrappings); in hopes of improving the differentiation of teeth from skull. Despite teeth and skull being similar in composition, a difference exists in the ratio of the most attenuating components Ca and P, in dentin, and in the mandible, which we hope to exploit. Dentin is on average composed of 9 and 6 % by weight of Ca and P, while the mandible is on average composed of 30 and 13 % by weight of Ca and P, respectively.[9,10] The ratio

differences between dentin and the mandible in Ca and P may improve differentiation of teeth from skull using dual-and triple-energy algorithms developed in chapter 3.

An initial triple-energy decomposition into teeth and skull as seen in **Figure 4-2** (b, c) shows an improvement in distinguishing teeth from skull versus a traditional MIP image taken at 80 kVp **Figure 4-2** (a). In addition, the arrow in **Figure 4-2** (b) shows the presence of what could be a supernumerary tooth (not seen in a typical MIP), which would be an unusual observation, if it can be confirmed.

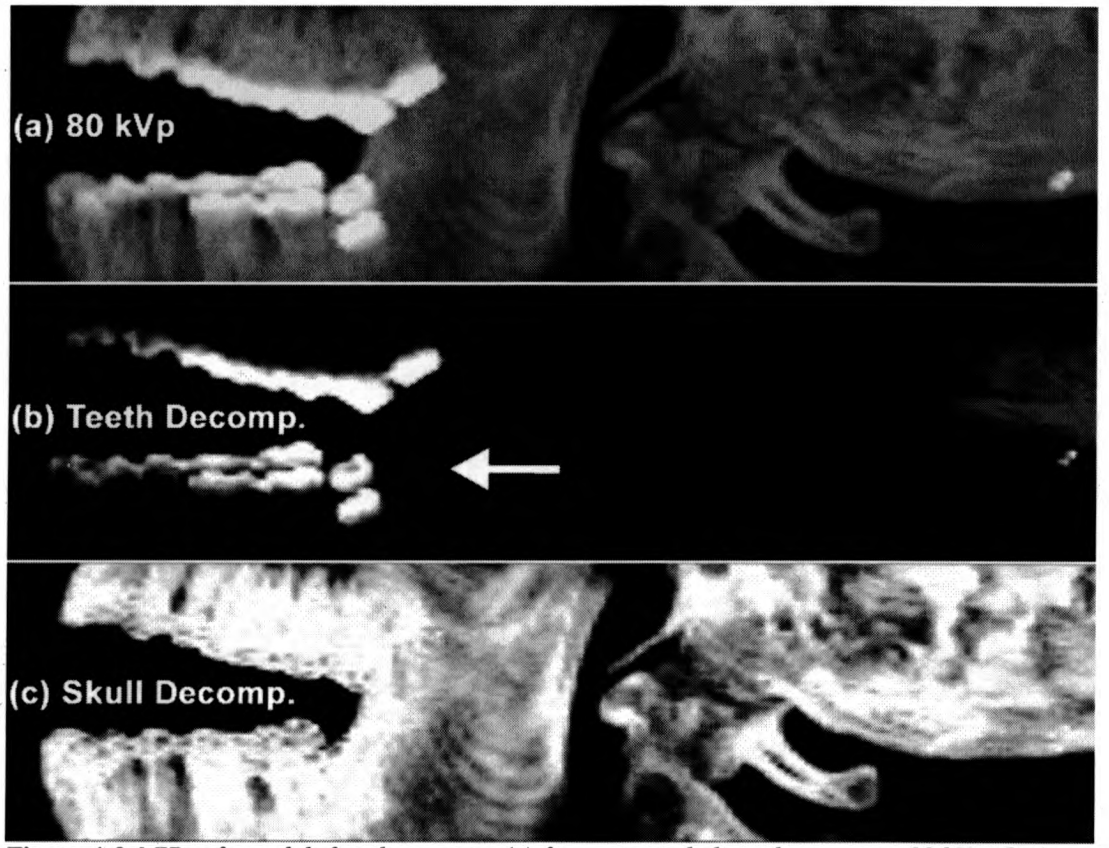

Figure 4-2 *MIPs of an adult female mummy, (a) from a typical clinical scanner at 80 kVp, (b-c) using a triple-energy decomposition into teeth (b) and skull (c). Arrow indicates what could be a supernumerary tooth.*

4.3 Conclusion

In this thesis, I have described new techniques to extend the capabilities of quantitative micro-CT imaging in research protocols. Using either *singe-energy* or multi-energy CT, I have shown that it is possible to classify tissue components – and added contrast agents – with high accuracy and precision. These techniques have been implemented on conventional CT equipment, and can be widely adopted by other research groups, potentially having a significant impact on pre-clinical imaging research programs throughout the world.

4.4 References

1 Kevin Eng, Rangaraj Mandayam Rangayyan, Robert Charles Bray, Cyril Basil Frank, Linda Anscomb, and Pamela Veale, "Quantitative analysis of the fine vascular anatomy of articular ligaments", IEEE Transactions on Biomedical Engineering **39**, 296-306 (1992).

2 D. D. McErlain, C. T. Appleton, R. B. Litchfield, V. Pitelka, J. L. Henry, S. M. Bernier, F. Beier, and D. W. Holdsworth, "Study of subchondral bone adaptations in a rodent surgical model of OA using in vivo micro-computed tomography", Osteoarthritis Cartilage **16**, 458-469 (2008).

3 J. R. Vetter, W. H. Perman, W. A. Kalender, R. B. Mazess, and J. E. Holden, "Evaluation of a prototype dual-energy computed tomographic apparatus. II. Determination of vertebral bone mineral content", Med Phys **13**, 340-343 (1986).

4 W. A. Kalender, W. H. Perman, J. R. Vetter, and E. Klotz, "Evaluation of a prototype dual-energy computed tomographic apparatus. I. Phantom studies", Med Phys **13**, 334-339 (1986).

5 R. E. Alvarez, J. A. Seibert, and S. K. Thompson, "Comparison of dual energy detector system performance", Med Phys **31**, 556-565 (2004).

6 F. Kelcz, P. M. Joseph, and S. K. Hilal, "Noise considerations in dual energy CT scanning", Med Phys **6**, 418-425 (1979).

7 T. G. Flohr, C. H. McCollough, H. Bruder, M. Petersilka, K. Gruber, C. Suss, M. Grasruck, K. Stierstorfer, B. Krauss, R. Raupach, A. N. Primak, A. Kuttner, S. Achenbach, C. Becker, A. Kopp, and B. M. Ohnesorge, "First performance evaluation of a dual-source CT (DSCT) system", Eur Radiol **16**, 256-268 (2006).

8 C. Rist, T. R. Johnson, A. Becker, A. W. Leber, A. Huber, S. Busch, C. R. Becker, M. F. Reiser, and K. Nikolaou, "[Dual-source cardiac CT imaging with improved temporal resolution: Impact on image quality and analysis of left ventricular function]", Radiologe **47**, 287-290, 292-284 (2007).

9 Maria del Pilar GutiÈrrez-Salazar and Jorge Reyes-Gasga, "Microhardness and chemical composition of human tooth", Materials Research **6**, 367-373 (2003).

10 D. R. White, "Tissue substitutes in experimental radiation physics", Med Phys **5**, 467-479 (1978).